The Astrophysical Journal, 938:116 (22pp), 2022 October 20 https://doi.org/10.3847/1538-4357/ac8eaa

First Flight of the EUV Snapshot Imaging Spectrograph (ESIS)

Jacob D. Parker[1], Roy T. Smart[1], Charles Kankelborg[1], Amy Winebarger[2], and Nelson Goldsworth[1]
[1] Montana State University, Culbertson Hall, 100, Bozeman, MT 59717, USA
[2] NASA Marshall Space Flight Center, Martin Rd SW, Huntsville, AL 35808, United States

Received 2022 April 7; revised 2022 August 12; accepted 2022 August 23; published 2022 October 19

Abstract

The Extreme-ultraviolet Snapshot Imaging Spectrograph (ESIS) launched on a sounding rocket from White Sands Missile Range on 2019 September 30. ESIS is a computed tomography imaging spectrograph (CTIS) designed to map emission line profiles across a wide field of view, revealing the structure and dynamics of small-scale transient events that are prevalent at transition region temperatures. In this paper, we review the ESIS instrument, mission, and data captured. We demonstrate how this unique data set can be interpreted qualitatively and further present some initial quantitative inversions of the data. Using a multiplicative algebraic reconstruction technique, we combine information from all four ESIS channels into a single spatial–spectral cube at every exposure. We analyze two small explosive events in the O V 629.7 Å spectral line with jets near $\pm 100\ \mathrm{km\ s^{-1}}$ that evolve on 10 s timescales and vary significantly over small spatial scales. Intriguingly, each of these events turns out to be a bimodal (red+blue) jet with outflows that are asymmetric and unsynchronized. We also present a qualitative analysis of a small jetlike eruption captured by ESIS and draw comparisons to previously observed mini-filament eruptions. In 5 minutes of observing time, ESIS captured the spatial and temporal evolution of tens of these small events across the $\sim 11\rlap{.}'5$ field of view, as well as several larger extended eruptions, demonstrating the advantage of CTIS instruments over traditional slit spectrographs in capturing the spatial and spectral information of dynamic solar features across large fields of view.

Unified Astronomy Thesaurus concepts: Spectroscopy (1558)

Supporting material: animations

1. Introduction

Observationally, the solar transition region refers to the portion of the solar atmosphere at temperatures between 20,000 and 800,000 K. Initially, the transition region was viewed as simply the thin interface region between the dense, cool chromosphere and tenuous, million-degree corona, where the temperature of the plasma dramatically increased 2 orders of magnitude over tens of kilometers (see Tian 2017, and references therein). Though this type of transition region undoubtedly exists in hot coronal loops, the concept of the transition region has been expanded over the last 20 yr to include a dynamic and complicated three-dimensional geometry.

The transition region is rife with magnetically driven phenomena such as explosive events (e.g., Dere et al. 1991) and microflares (Gontikakis & Winebarger 2012), which manifest supersonic flows. Explosive events were discovered in rocket flights (Dere et al. 1989) and exhibit Doppler broadening of order $\pm 100\ \mathrm{km\ s^{-1}}$. The release of free magnetic energy in the low-β plasma was implicated because these flows are much faster than the transition region sound speed (e.g., $\approx 55\ \mathrm{km\ s^{-1}}$ for C IV, formed at 10^5 K). Innes et al. (1997) found fast bidirectional jets in Si IV 1394 Å line profiles taken by the Solar Ultraviolet Measurements of Emitted Radiation instrument (Wilhelm et al. 1995) separated by a few arcseconds and inferred that they must be associated with the outflows of an inclined reconnection current sheet. Higher-resolution observations from the Interface Region Imaging Spectrograph (IRIS; De Pontieu et al. 2014) have shown that Si IV line profiles often show very bright line cores with broad wings and very non-Gaussian, more triangular profiles. This enhanced line core emission points to a larger amount of stationary plasma and has been attributed to reconnection by the tearing mode instability (Innes et al. 2015). Enhanced emission in the line core of a larger explosive event viewed in He II 304 Å by the Multi-Order Solar Extreme-ultraviolet Spectrograph (MOSES) has also been attributed to the tearing mode instability (Fox et al. 2010), but tens of smaller events in the same data have clear bimodal profiles (Rust & Kankelborg 2019). In order to determine which, if any, of these presentations is typical, we require high-cadence velocity data over a wide range of temperatures simultaneously, something difficult to achieve even in multi-instrument studies.

Investigations of transition region events to date are severely limited by the available observational capabilities. Historically, slit spectrographs have been used to determine the velocity of the plasma in the solar atmosphere. Spectrally resolved images of the sky plane must be built by rastering the slit over the region of interest, which takes much longer than the timescales of the transition region phenomena and confuses whether events are evolving temporally or varying spatially. In order to fully capture the velocity distribution and temporal evolution of quickly evolving solar events, particularly those with larger spatial extents, we require imaging instruments capable of gathering spectra in every pixel over a large field of view at every exposure.

One solution to simultaneously capturing spatial and spectral information over a large field of view is to use a slitless imaging spectrograph. The data from these instruments, sometimes called overlapograms, have spatial and spectral information overlapped in the dispersive direction, requiring the data to be inverted or unfolded. The difficulty in unfolding slitless spectrograph data has limited its usefulness for extended astrophysical objects like the Sun. Only two satellite missions have routinely captured solar slitless spectrograph data, the S082A instrument on Skylab (Tousey et al. 1973) and the Res-K instrument of the Russian KRONOS-I mission (Zhitnik et al. 1998), though others have recently been developed and proposed (Winebarger et al. 2019; Golub et al. 2020). Additionally, the currently operating Extreme-ultraviolet Imaging Spectrograph (EIS; Culhane et al. 2007) on the Hinode mission (Kosugi et al. 2007) includes 40″ and 266″ slots that can produce overlapogram data. Though EIS slot data are not often studied quantitatively, they have been used as a flare-mode trigger and since analyzed to aid in interpretation of the impulsive phase of solar flares (Harra et al. 2017, 2020). In addition to these satellite observatories, the MOSES instrument by Kankelborg and collaborators (Kankelborg & Thomas 2001; Fox et al. 2010; Rust & Kankelborg 2019) has observed dynamic events in the solar transition region. MOSES captured the zero and ±1 orders of the He II 304 Å line simultaneously. Doppler shifts were then detected as the spectral displacements in opposite directions in the ±1 orders.

Slitless spectrograph data can be thought of as a projection of a three-dimensional spatial–spectral data cube, $I(x, y, \lambda)$, onto a two-dimensional detector. Although Skylab S082A had just a single projection through x, y, λ-space, it was possible under some circumstances to determine line intensities and ratios (e.g., Keenan et al. 1988, 2006; Tayal et al. 1989) and even Doppler shifts (Mariska & Dowdy 1992). Slitless spectrographs using two projections (usually one dispersed and one undispersed) have proven sufficient to implement an efficient ground-based magnetograph (DeForest et al. 2004), map Doppler shifts in the solar transition region (Courrier & Kankelborg 2018), and invert temperature or density information (Winebarger et al. 2019). However, as with any tomographic inversion problem (e.g., Kak & Slaney 2001), the fidelity of reconstruction improves dramatically as projections are added. This is particularly true as the complexity of the object increases, causing the overlap of multiple features along the projection. An instrument that captures multiple projections of the spatial–spectral data cube is called a computed tomography imaging spectrograph (CTIS; Descour & Dereniak 1995). MOSES is an example of a CTIS, as it captured three projections in the ±1 and zero orders. Fox et al. (2010) were able to extract line widths and Doppler shifts from a relatively complex explosive event observed by MOSES in He II 304 Å. Rust & Kankelborg (2019) found unambiguous evidence of explosive events with well-resolved, double-peaked spectral line profiles in the same data set.

The Extreme-ultraviolet Snapshot Imaging Spectrograph (ESIS) is a CTIS with four unique projections of the spatial–spectral data cube and is designed to capture velocity information in small-scale reconnection events in the O V 629.7 Å emission line that is formed in the solar transition region. ESIS builds off of the MOSES concept but adds an additional projection and an explicit field of view defined by the field stop, a significant upgrade in flexibility and data quality over MOSES. ESIS was launched along with MOSES from White Sands Missile Range on 2019 September 30. Unfortunately, the MOSES shutter failed to open during the flight and did not collect any solar images as a result. In this paper, we will describe the ESIS mission and data and show a preliminary analysis of several observed events. We will demonstrate that ESIS is capable of measuring velocity over a wide field of view at a rapid cadence in a way no slit spectrograph can.

Table 1
Dominant Spectral Lines Observed by ESIS

Ion	λ (Å)	Intensity
He I	584.33	0.70
O III	599.59	0.13
O IV	608.40	0.06
Mg X	609.79	0.25
O IV	609.83	0.11
Mg X	624.94	0.13
O V	629.73	1.00

Note. Intensities are relative to O V 629.7 Å.

The ESIS experiment, target, and flight are described in Section 2. Section 3 provides information on the data processing. Preliminary results are given in Section 4; these include both qualitative and quantitative measures of small-scale velocity events in the solar transition region. The ESIS mission was successful in observing tens of small-scale reconnection events over the short rocket flight, as well as demonstrating the usefulness of CTIS observations and developing the analysis techniques required to interpret these unique data.

2. ESIS Mission

In this section, we provide an overview of the ESIS experiment, as well as the time and conditions of the ESIS rocket launch and subsequent data collection.

2.1. The Experiment

The full ESIS experiment includes an optical instrument, a set of detectors, an onboard data acquisition system, and ground support equipment and is described in great detail in the preceding paper (Smart et al. 2022). The ESIS optical design consists of a single parabolic primary mirror, an octagonal field stop placed at prime focus, and four spherical diffraction gratings each with their own corresponding CCD detector. Incoming light is focused by the primary mirror onto the octagonal field stop. The octagonal field stop is approximately 5 mm wide, which is equivalent to 11$'\!.$5 when projected onto the sky. The light that exits the field stop is reimaged by each of four spherical diffraction gratings onto its own CCD. The portion of the solar spectrum that is captured by each detector ranges from approximately 584 to 630 Å. Table 1 shows the dominant lines observed by ESIS. Intensities relative to O V 629.7 Å are calculated using Chianti (Dere et al. 1997; Del Zanna & Young 2020) assuming a constant pressure of 10^{15} K cm^{-3} and a quiet Sun DEM, combined with the Schmeltz 2012 abundance file (Schmelz et al. 2012). While this paper focuses primarily on the dominant O V 629.7 Å spectral line, future work will be focused on measuring plasma velocity in other bright lines.

Each grating and detector pair, referred to as a channel in this paper, is itself an independent slitless imaging spectrograph. The channels are arrayed at 45° increments about the axis of symmetry of the paraboloidal primary mirror such that each channel disperses the solar image in a different direction. Hence, each of these channels captures a unique projection of the spatial–spectral cube, shown in Figure 1. As shown, each channel captures the Sun imaged through the octagon and dispersed at different relative angles with respect to solar north. Exposures from all four channels are gathered nearly

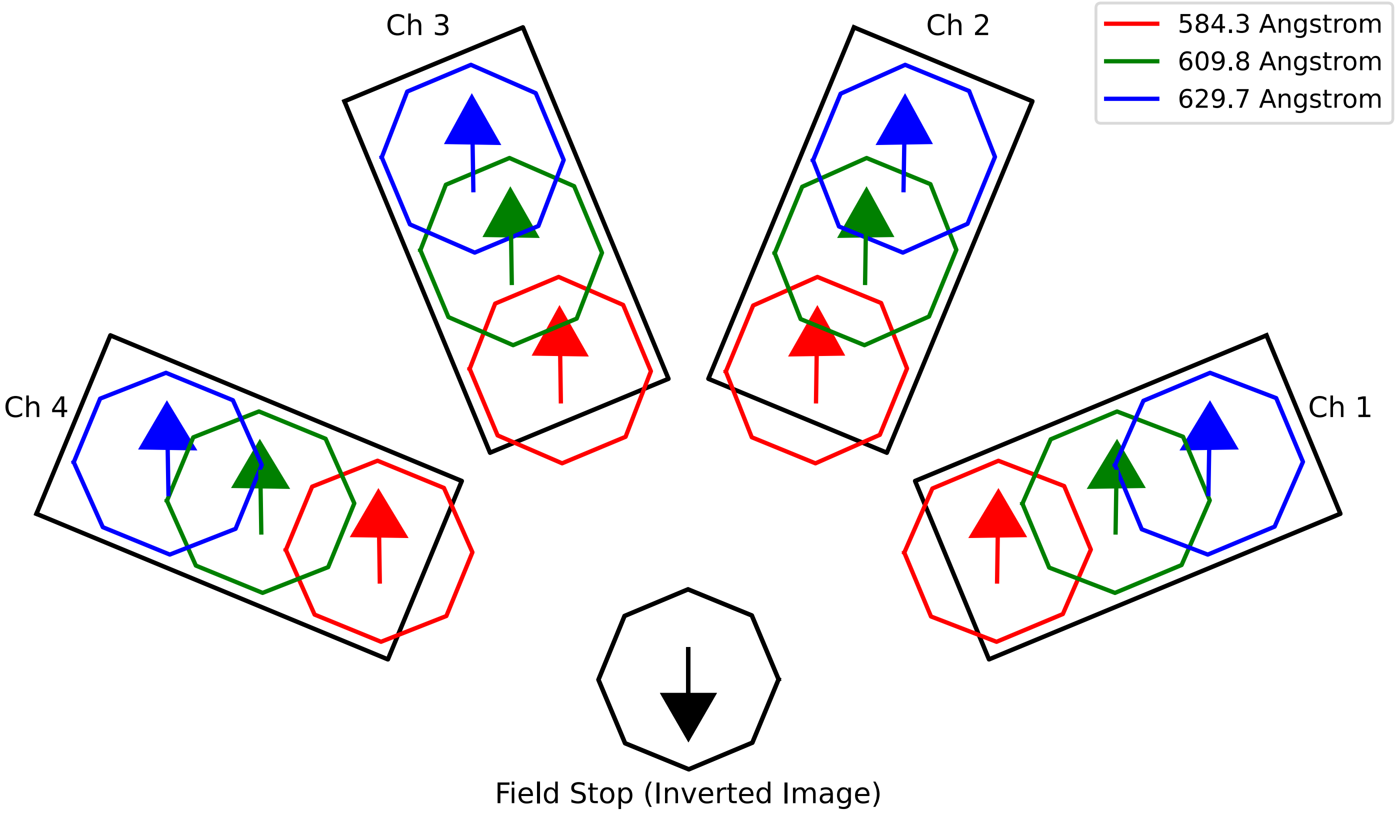

Figure 1. Modeled layout showing the orientation of each ESIS channel's detector relative to the solar image at the octagonal field stop. The locations of the brightest wavelengths (He I 584.3, Mg X 609.79, and O V 629.7 Å) in the passband are shown on each detector. The He I 584.3 Å line extends off the detector edge by design, as can be seen in Figure 2.

simultaneously by triggering the frame transfer in three of the cameras by a single "master" camera. Simultaneously imaging with multiple slitless spectrographs with different dispersion directions is what makes ESIS a CTIS. The ESIS instrument currently has four channels but is built to accommodate up to six (limited by interference with the optical bench).

2.2. Launch and Data Collection

ESIS was launched at 18:04:00 UTC on 2019 September 30 from White Sands Missile Range. Figure 3 provides the height of the sounding rocket as a function of time determined from radar measurements, as well as several key events during the flight. The ESIS cameras began exposing at launch and continued to record full detector ($\sim 2k \times 1k$) images with a 10 s exposure and cadence throughout the flight. Images taken while the experiment shutter door was closed (i.e., during the initial boost phase of the rocket flight and ballistic ascent to approximately 100 km altitude) serve as darks. At 73.0 s after launch, the shutter door opened. The Sun was acquired by the Solar Pointing And Rocket Control System (SPARCS), and the ring laser gyro (RLG) was enabled at 124.2 s, indicating the rocket was in fine-pointing mode. During this mode, SPARCS maintained a constant target; however, thermal expansion of optical components inside the instrument caused the apparent drift of the solar image on the detectors, as described in Section 3. At 433.0 s, the shutter door closed, ending solar observations. Exposures continued until the system shut down at 18:15:41, providing several additional dark frames at the end of the flight. A summary of the flight and data collected is given in Table 2.

On the Sun, 2019 September 30 was a very quiet day. The last B-class event detected by GOES (Chamberlin et al. 2009) prior to the ESIS launch was on 2019 July 7. Because of this exceptionally quiet period on the Sun, we chose to point at disk center. The actual pointing of the center of the ESIS octagonal field stop and roll were found after flight by comparing the ESIS exposure nearest apogee at 18:08:17 UTC to the closest 304 Åimage in time taken by the Atmospheric Imaging Assembly (AIA; Lemen et al. 2012), at 18:08:17 UTC. The ESIS field of view projected onto the AIA 304 Å image is shown in Figure 4 as a green octagon. The pointing was found to be $\sim[18'', -19'']$, and the roll offset was found to be $\sim 0\overset{\circ}{.}85$ (clockwise about Sun center), both within the tolerances for SPARCS pointing. Figure 4 shows the full-disk AIA 304 Å image. The ESIS field of view is indicated by the octagon.

Each of the ESIS cameras collected 71 images during flight. The first two images are unusable; the first image has an exposure time of 0 s and is basically a dump of the dark current in the camera, while the second image has an exposure time slightly longer than 10 s caused by the cameras syncing to a single trigger of the master camera. All of the other images have a 10 s exposure time. Twenty-nine of these images were light frames, meaning that the shutter door was open and the RLG was enabled. The time during the rocket flight when light frames were collected is shaded green in Figure 3. Light emitted by the Sun is absorbed by the Earth's atmosphere. The degree of absorption depends upon the column of the atmosphere that the telescope is looking through. The wavelength dependence of atmospheric absorption is weak, on the order of a few percent across the ESIS passband. Figure 3 shows the mean intensity in each of the ESIS channels

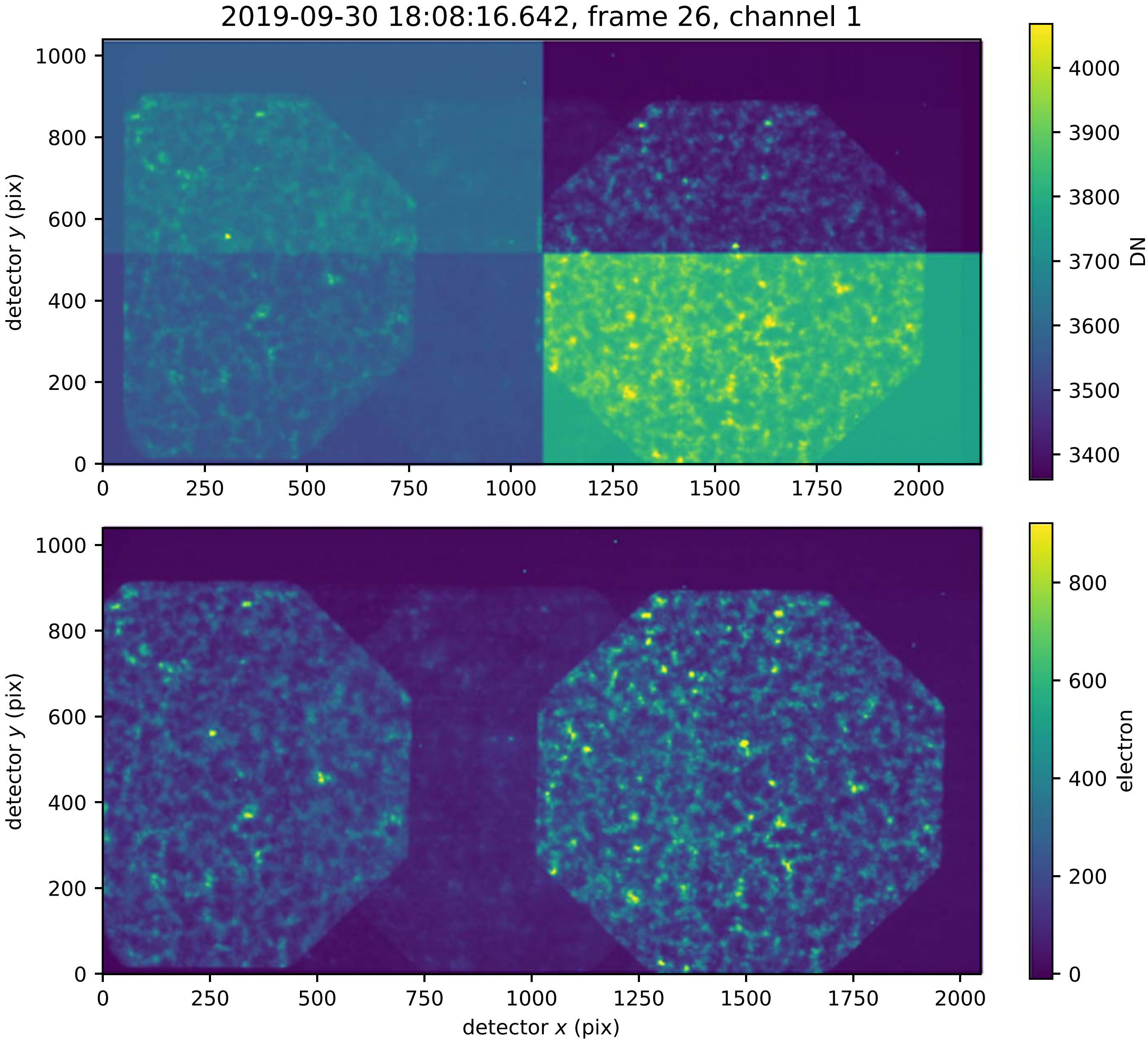

Figure 2. The top panel is the raw, level 0 image captured by channel 1 of ESIS during apogee. The bottom panel is the same image after level 1 processing. The Sun viewed through the octagonal field stop in the O V 629.7 Å spectral line is on the right side of the detector; this portion of the detector was cropped to generate level 3 data. The Sun viewed through the octagonal field stop in the He I 584.3 Å line is partially on the left side of the detector. The Mg X 609.79 Å line is between and partially overlapping both of these strong lines.

as a function of time. Atmospheric absorption clearly impacted the observations in the up- and downlegs of the flight. Accounting for atmospheric absorption will be discussed in Section 3. Though there are 29 light frames, the first and last several frames were greatly impacted by atmospheric absorption and have limited usefulness. As the rocket was reentering the atmosphere, a transient signal affected some of the images that would otherwise be considered darks. It is likely due to violent deceleration when the payload encountered Earth's atmosphere. This effect can be seen as the small bump in the mean intensities at roughly 18:12:20 in Figure 3. We restrict the dark frames to the data taken after the first two images but before the shutter door opened in the upleg and after the transient in the downleg; these times are shaded gray in Figure 3. In total, there were 20 usable dark images.

3. Data

We have established several levels of data processing that are described in detail below. Level 0 represents the raw data that were obtained by the four different cameras during flight. Level 1 data incorporate a quadrant-dependent bias and gain correction, cropping of nonactive pixels (NAPs), and dark subtraction. Normally, for solar observatories like AIA, higher-level data would be further corrected for solar pointing and roll by interpolating the data onto a common grid referenced to solar coordinates (Lemen et al. 2012). For ESIS, this step would be complicated and would not be the best treatment of the data. First, the spatial–spectral overlap on the detector complicates the notion of image alignment. Second, interpolation inherent in such geometrical corrections degrades spatial resolution unnecessarily. Finally, the ESIS optics slightly

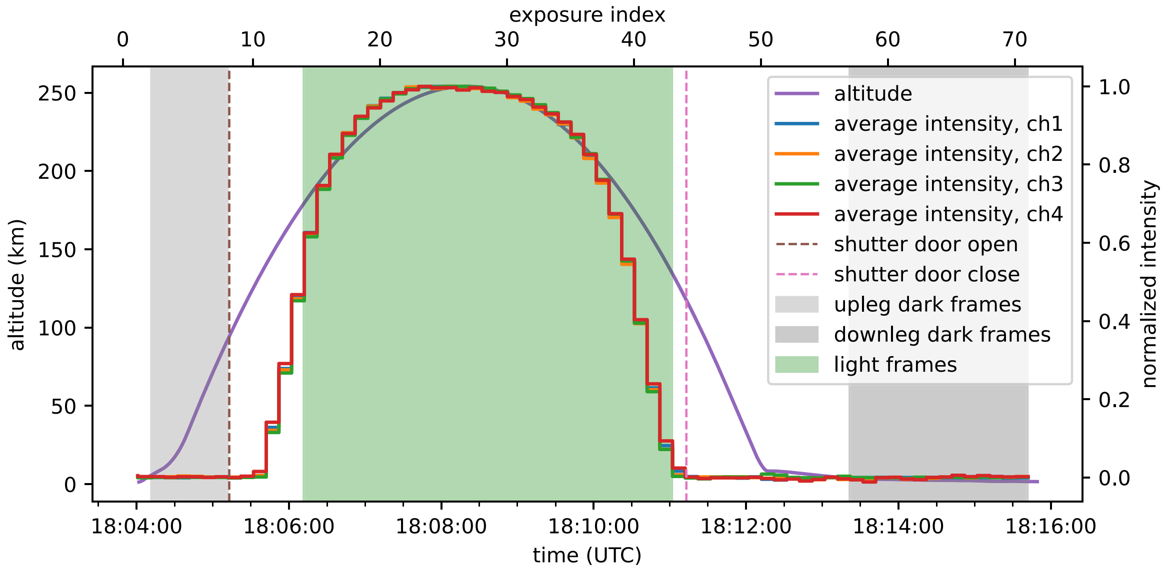

Figure 3. Altitude of the ESIS rocket determined from White Sands Missile Range radar data as a function of elapsed time from launch. The event times listed in Table 2 are labeled.

Table 2
ESIS Flight Data Summary

Launch date	2019 September 30	Image size	(1040, 2048) pixels
Data acquisition time	18:04:00–18:15:41 UTC	Avg. noise	4.02 ± 0.14 DN
Pointing	≈[18″, −19″]	Avg. gain	2.56 ± 0.03 e^- DN^{-1}
Field of view	≈11′.5 octagonal	Exposure time	10 s
Roll	≈0°.85 CW	No. light exp.	29
Spatial plate scale	[0″.74, 0″.77] pixel^{-1}	No. dark exp.	20
Spectral plate scale	0.037 Å pixel^{-1}		

distort the solar image, mainly due to the tilt of each CCD and also anamorphic magnification by the gratings, which occurs along the dispersion direction for each channel. In fact, the distortion is a nontrivial function of both position and wavelength (Smart et al. 2022), so that it cannot be undone in two dimensions. It must be addressed by simultaneously inverting the spatial–spectral cube across all wavelengths. Because of this complication, we define two additional data levels.

Level 2 data will include updated header information with accurate coefficients of a nonlinear and wavelength-dependent coordinate mapping from solar coordinates and wavelength to each detector for each image. As we have noted, ESIS images cannot be straightforwardly distortion-corrected prior to distribution. Therefore, we will distribute the distortion parameters needed to forward model from a spatial–spectral cube to each ESIS detector, which are essential to inverting for the full ESIS passband. Each image will be corrected for differing levels of absorption from the Earth's atmosphere during the course of the flight and contain a header keyword tracking the correction as a function of time for use in instrument noise models. In addition, level 2 data will be despiked and stored with a mask of spike locations for future respiking. Level 2 data are a necessary step toward inverted data products that cover the full ESIS wavelength range. The level 2 distortion model must incorporate the optical design parameters and the consequences of small element-by-element misalignments that inevitably occur when an optical system is built up. This model is in active development and is not described further here.

In lieu of a complete level 2 product, we seek a shortcut to interpretation of the ESIS data, which we will refer to as level 3. Level 3 data are comprised of a single spectral line cropped from level 1 data and mapped to the sky plane via a nonlinear coordinate transform derived from a coalignment to cotemporal AIA data and an internal coalignment of each ESIS channel to a reference channel. Over the short wavelength range corresponding to a single spectral line (for our present purpose, we will choose O V 629.7 Å), the wavelength dependence of the ESIS distortion function is negligible, and the spatial distortion can be corrected by comparing ESIS data to cotemporal AIA 304 Å data. This shortcut allows us to take differences between images and perform simplified inversions that are nevertheless rich in physical detail.

The level 0, 1, and 3 data products are described in detail in the remainder of this section.

3.1. Level 0 Data

Level 0 data are the raw data collected during the ESIS rocket flight. Each image was written to a FITS file with onboard time stamp, camera number, and other parameters, such as the readout from temperature sensors included in the header.

Each camera includes a detector with 2048 columns and 2064 rows. The detector is operated in frame transfer mode, meaning the exposed portion of the detector is shifted into a storage portion that is read out during the next exposure. The storage portion is simply a mechanically masked region of the detector. The intention was that the storage region would be

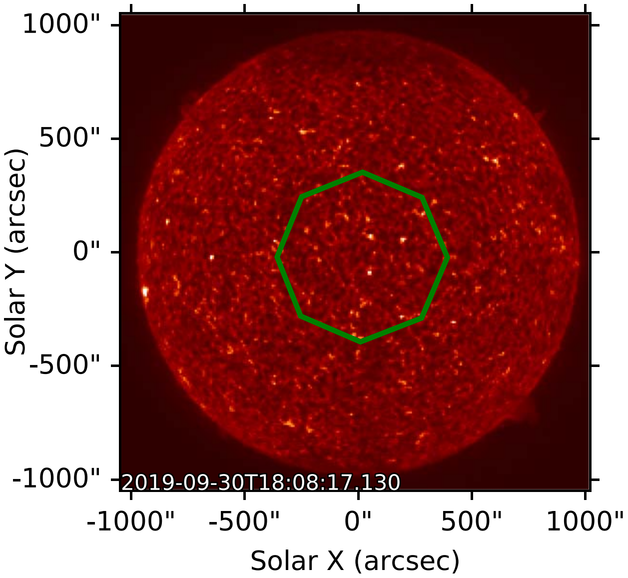

Figure 4. Reference AIA 304 Å data taken at 18:08:17 UTC used for determining the absolute pointing. The octagon indicates the ESIS field of view.

520 rows per quadrant, while the exposed region would be 512 rows per quadrant, producing an image that was 1024 rows in total. An oversight during implementation inverted the size of the storage and exposed region, meaning the final image had 1040 rows. Having a larger exposed region than storage region implies that eight rows originally exposed at the central portion of the detector were not behind the mechanical mask when the readout was initiated. However, because these rows were only unmasked for roughly 20 ms, as compared to the 10 s exposure time, there was no discernible impact on the data.

The data are read out through four ports, corresponding to the four quadrants of the detector. The readout register has 50 additional dummy pixels, or NAPs, that are read out before each row of the detector data. When the detector is read out, those 50 pixels are stored as part of the image. Two additional "overscan" pixels are read after each row of data and stored as part of the image. A level 0 data file, then, is 2152 × 1040 pixels. During preflight lab testing, it was found that the median intensity in columns 21–50 of the NAPs of each readout port are an excellent proxy for the detector bias. Additionally, the data from each port are converted from analog to digital through a unique circuit. Though the same components were used, slight variations in the circuits caused slight differences in the gain (elec/DN) and read noise associated with each quadrant. The gain for each quadrant in each camera was measured prior to flight. The gain enables us to relate DN to photons and calculate shot noise in each pixel. The readout noise was measured by calculating pixelwise standard deviations from usable dark images taken during flight and then averaging the standard deviation. These statistics are tabulated in Table 2.

3.2. Level 1 Data

A summary of the flight data parameters, as described in the preceding sections, is provided in Table 2. For each channel, there were 29 light images that were processed into level 1 data and 20 dark images used to process the data. Our procedure to convert from level 0 to level 1 is described below. An example of a level 0 and level 1 image is shown in Figure 2.

1. Calculate and subtract the bias of each quadrant of each usable image (light or dark) by taking the median of columns 21–50 of the NAPs for each readout port.
2. Create a master dark image for each channel by taking the median along the time axis of all of the bias-subtracted usable dark images.
3. Subtract the master dark from each bias-subtracted light image.
4. Crop each image to remove the NAPs and overscan pixels.
5. Convert images from DN to electrons by multiplying each quadrant of each image by the gain for that quadrant.

The resulting level 1 data set contains each channel's image sequence in units of photoelectrons. In addition to the images, the level 1 header is updated with the time, exposure length, and altitude associated with each image using standard FITS header keywords.

3.3. Level 3 Data

The ESIS level 3 data product is created to provide a coaligned, single-wavelength image in each channel for quick identification of events with significant line-of-sight velocities and easy comparison with coordinated data that do not require inversion. Level 3 data also allow for single-wavelength inversion prior to the completion of the final optical distortion model and the level 2 data product. A demonstration of both qualitative and quantitative analysis of level 3 data is given in Section 4.

Level 3 data are generated directly from level 1 as follows.

1. Level 1 data are converted to units of photons in the target wavelength and then despiked.
2. Optical distortion and internal coalignment are corrected, and each channel is resampled onto an appropriately cropped common grid with known alignment to AIA data.
3. Each channel is corrected for vignetting.

Figure 5(a) shows an example of a level 3 image from channel 2 taken at 18:08:46. All three steps depend on the assumption that the intensities are associated with the target wavelength. No attempt is made to distinguish the photons of other wavelengths that may overlap with the octagonal field stop image in the target wavelength, so level 3 is a useful construct for a target wavelength corresponding to a strong spectral line with minimal contamination. The above steps are described in greater detail below.

3.3.1. Conversion to Photons and Despiking

The conversion from electron to photon is done to level 1 data prior to coalignment efforts. The image intensity in the photons, I_γ, then becomes

$$I_\gamma = I_e * 3.6\frac{\text{eV}}{e} * \frac{\lambda}{hc}, \qquad (1)$$

where I_e is the level 1 image intensity in electrons, and λ is the target wavelength. With a silicon band gap energy of 3.6 eV e^{-1} and an energy per O V 629.7 Å photon of 19.6 eV, this gives 0.18 photons electron$^{-1.}$

Due to geomagnetic activity on launch day, our detectors received a substantial number of charged particle hits. We therefore elected to despike the data. Available despikers were

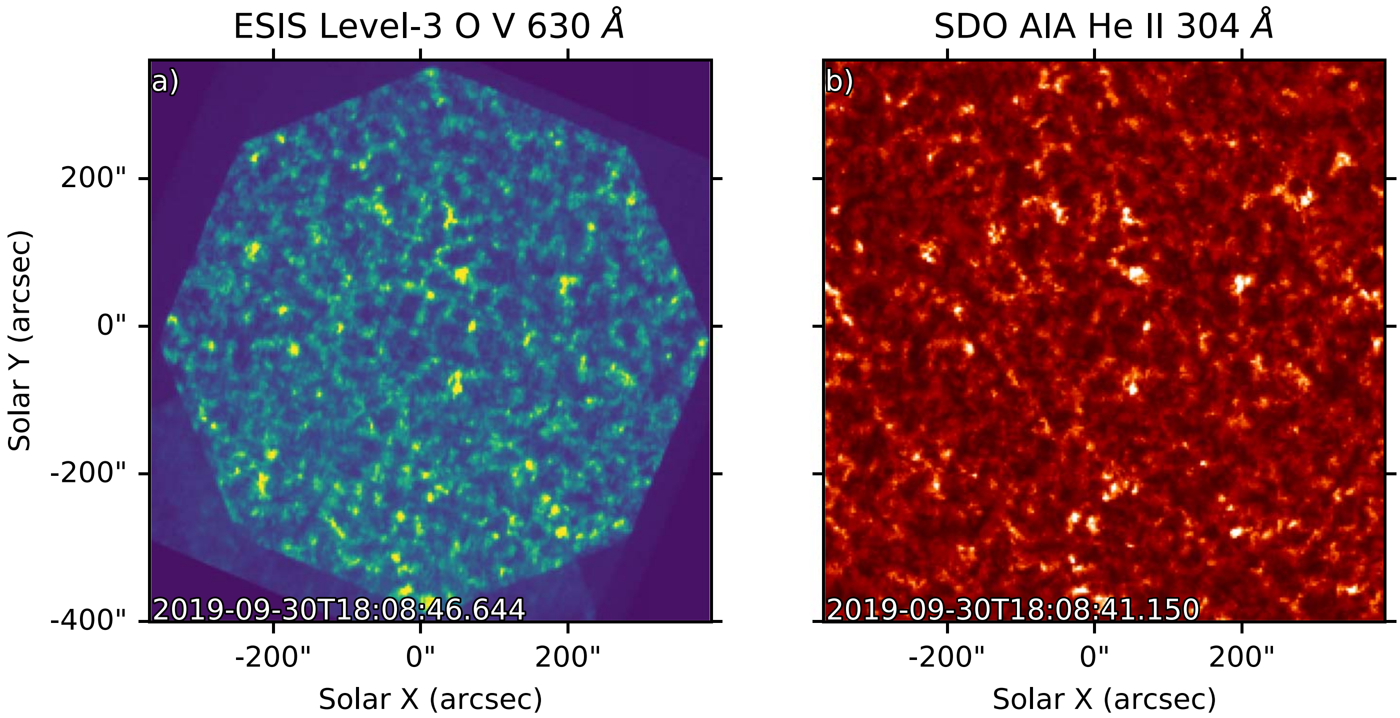

Figure 5. (a) Example of the level 3 data product from channel 1 taken at 18:08:46. These data have been aligned using linear mapping parameters to the closest cotemporal AIA 304 Å image, shown in panel (b).

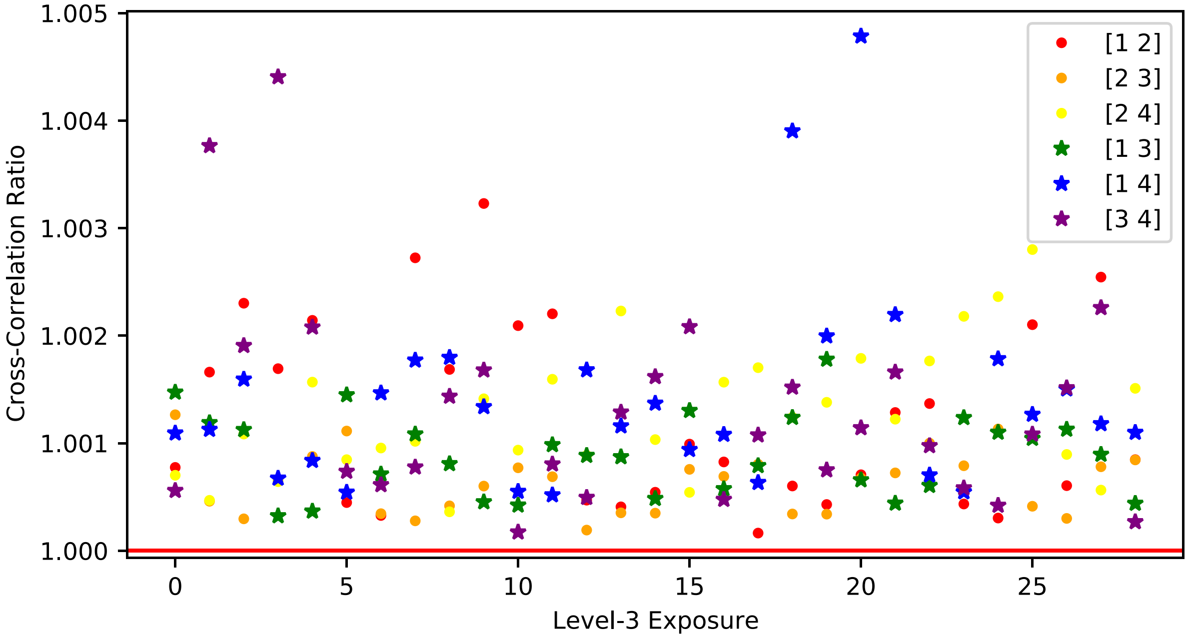

Figure 6. For each ESIS exposure (or image sequence), every channel pair, labeled in the legend, is cross-correlated to measure the internal alignment quality. The ratio of zero-lag cross-correlation after a quadratic transformation to that of a linear transformation is plotted. Every point is above the ratio = 1 line, indicating improved internal alignment for every combination of ESIS channels at each exposure.

difficult to tune in such a way that they eliminated particle hits but not small transient events (e.g., explosive events). We therefore developed a new despiking algorithm, which is identified in Appendix A.

3.3.2. Optical Distortion Correction and Channel Coalignment

The four ESIS channels were spatially coaligned in two steps. First, each ESIS image is cropped around the O V 629.7 Å spectral line (roughly pixels 1000–2048 of the level 1 data shown in Figure 2) and then coaligned to the closest AIA 304 Å image in time. The AIA 304 channel was chosen for coalignment because it is the AIA EUV channel most visually similar to O V (Figure 5(b)). Prior to coalignment, each AIA image was prepped to level 1.5 using the aiapy routines `aiapy.calibrate.update_pointing()` and `aiapy.calibrate.register()`. The coalignment was achieved through a linear coordinate transformation of the cropped ESIS image that maximizes the

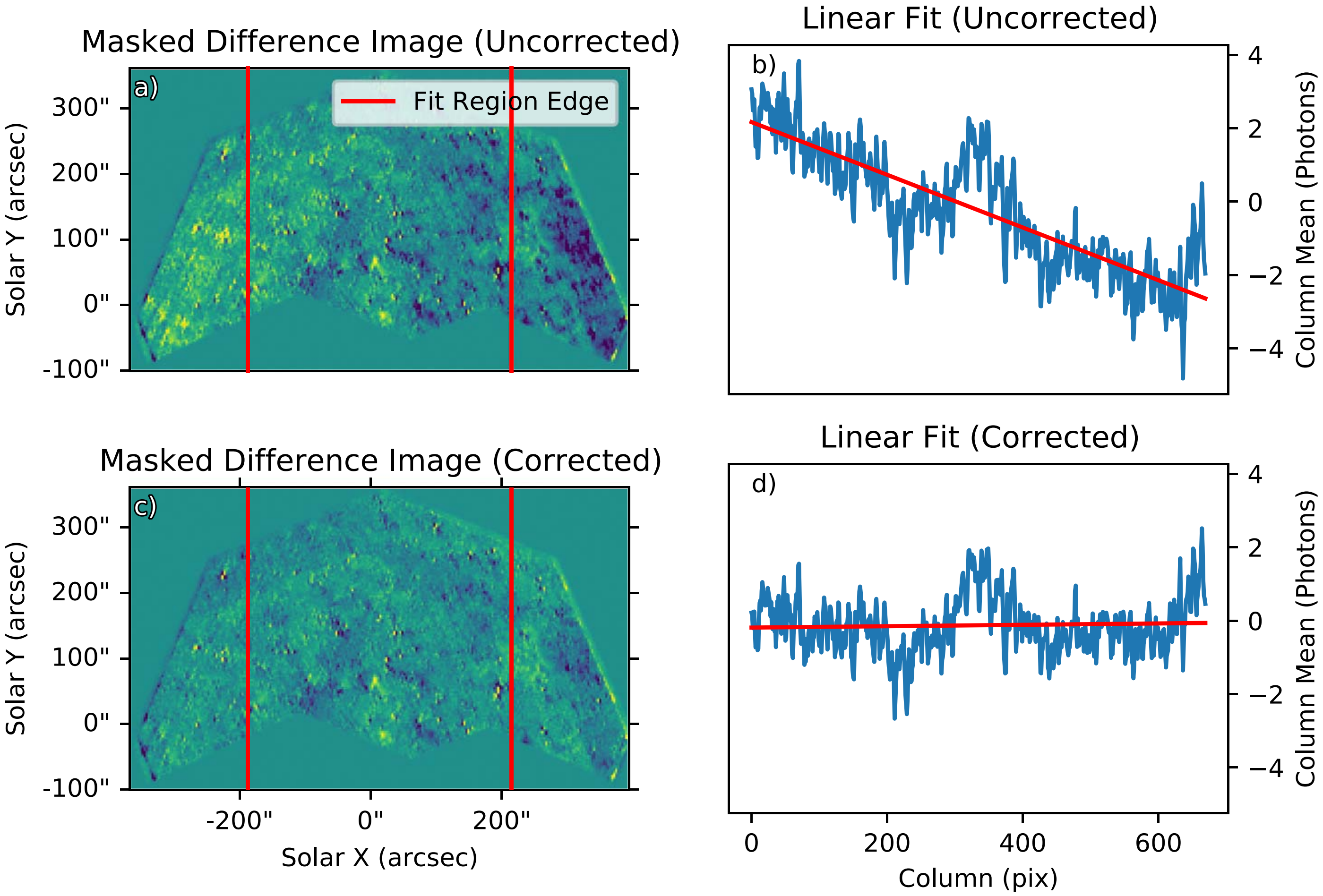

Figure 7. Panels (a) and (c) show examples of the difference between images with Mg X609.79Å masked that are uncorrected and corrected for vignetting, respectively. The line fit to the column mean as a function of the column (fit between the red bars) shows a difference in background of ≈five photons before correction (panel (b)) at the edges of the field of view and 0.4 photons after (panel (d)).

zero-lag cross-correlation between it and AIA 304. The results of this are shown in Figure 5. The mean correlation coefficient in this step is 0.26.

Since ESIS has a slightly nonlinear distortion function (Smart et al. 2022), an additional internal alignment step is performed. Subpixel accuracy of the ESIS interchannel alignment is critical to our tomographic inversion of the data to obtain line profiles, so we exercise more care than with the alignment to AIA. Using a single ESIS channel as reference, in this case channel 2, each other channel is coaligned to it via a quadratic coordinate transformation that maximizes the zero-lag cross-correlation. The mean correlation coefficient in this step is 0.92. Figure 6 shows the ratio of peak cross-correlation after the quadratic internal alignment to that of the linear coalignment with AIA for every camera pair and every exposure. A ratio greater than 1 implies that this second step improved coalignment. We find that the internal alignment improves both coalignment with the reference channel (dots in Figure 6) and the coalignment between every other combination of channels (stars in Figure 6). This ratio is greater than 1 in all cases and shows a less than 1% improvement in peak correlation, demonstrating the subtle nonlinearity of the ESIS optical distortion function. In pixels, this corresponds to an average change in mapping of ~0.4 pixels.

After the coalignment is complete, each level 3 image has been rebinned to AIA resolution, $0\farcs6$ pixel^{-1}, and can be assigned the WCS information (Calabretta & Greisen 2002) from the AIA image nearest in time, providing pointing information and easier coalignment with coordinating instruments. Image interpolation during coalignment is performed using a third-order spline interpolation, the current default of scipy.ndimage.map_coordinates.

3.3.3. Vignetting Correction

Each ESIS channel has a linear trend in intensity across the octagonal field of view along the dispersion direction due to internal vignetting caused by having multiple stops in the optical system (Smart et al. 2022). In the coaligned level 3 images, where solar north is rotated to the top of the image, the dispersion axes run at different angles relative to solar north in each channel, so the impact of the vignetting field can be seen in the linearly trending background when taking the difference between two channels (Figure 7(a)). We corrected the vignetting by dividing out a linearly trending background, aligned to the dispersion axis, in every image. The parameters of this trend in each channel were obtained by minimizing the intensity trend seen in level 3 difference images.

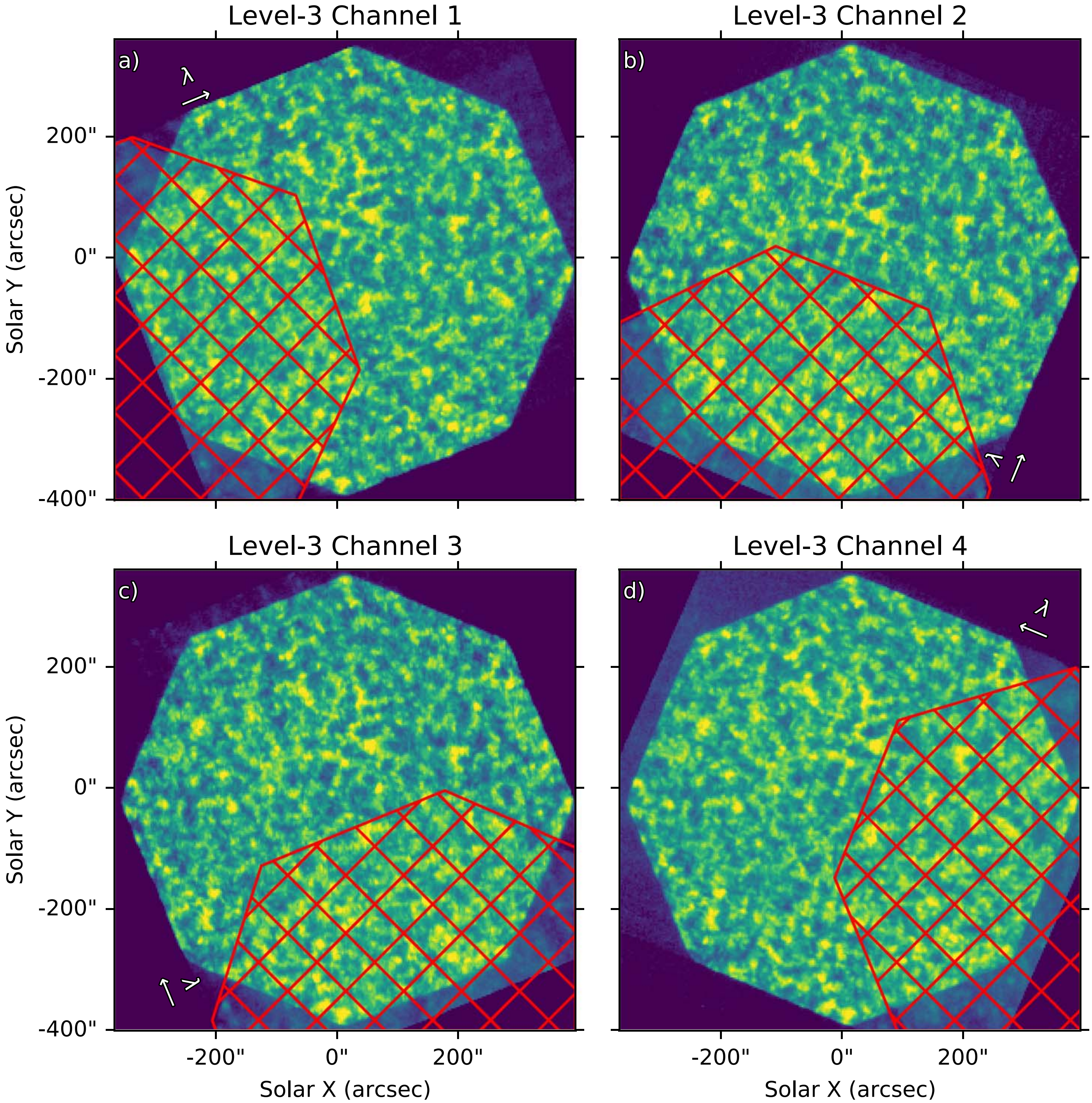

Figure 8. The red hatched region shows the overlap of the Mg X609.79 Å spectral line in each channel that is masked prior to the vignetting correction and intensity normalization. These images are displayed in log scale in an attempt to bring out the subtle contamination. The outline of the Mg X can be seen very clearly in difference images like Figure 9.

We define the vignetting field for the *i*th channel at each time index, *s*, as a function of the pixels in the level 3 data, (x, y), as

$$V_{is}(x, y) = \frac{m_i}{r_t} * [r(x, y, s) - r_0] + 1, \quad (2)$$

where

$$\begin{aligned} r = x_0 &+ [\cos(\alpha_i)(x - x_0 - x_{\mathrm{drift}} * s/s_t) \\ &- \sin(\alpha_i)(y - y_0 - y_{\mathrm{drift}} * s/s_t)]. \end{aligned} \quad (3)$$

In Equation (2), r_0 is equal to 65 pixels and represents the distance from the level 3 image edge to the ESIS field stop octagon edge at $s = 0$, the first level 3 image. The width of the octagon along the dispersion direction, r_t, is equal to 1140 pixels. In Equation (3), α_i is the angle of rotation of each ESIS level 3 image relative to a level 1 image row. In this case, $\alpha_i = [112^\circ\!.5, 67^\circ\!.5, 22^\circ\!.5, -22^\circ\!.5]$ for channels 1–4, respectively. The vignetting field is rotated about the point $[x_0, y_0] = [635, 635]$, which is the nominal center of the level 3

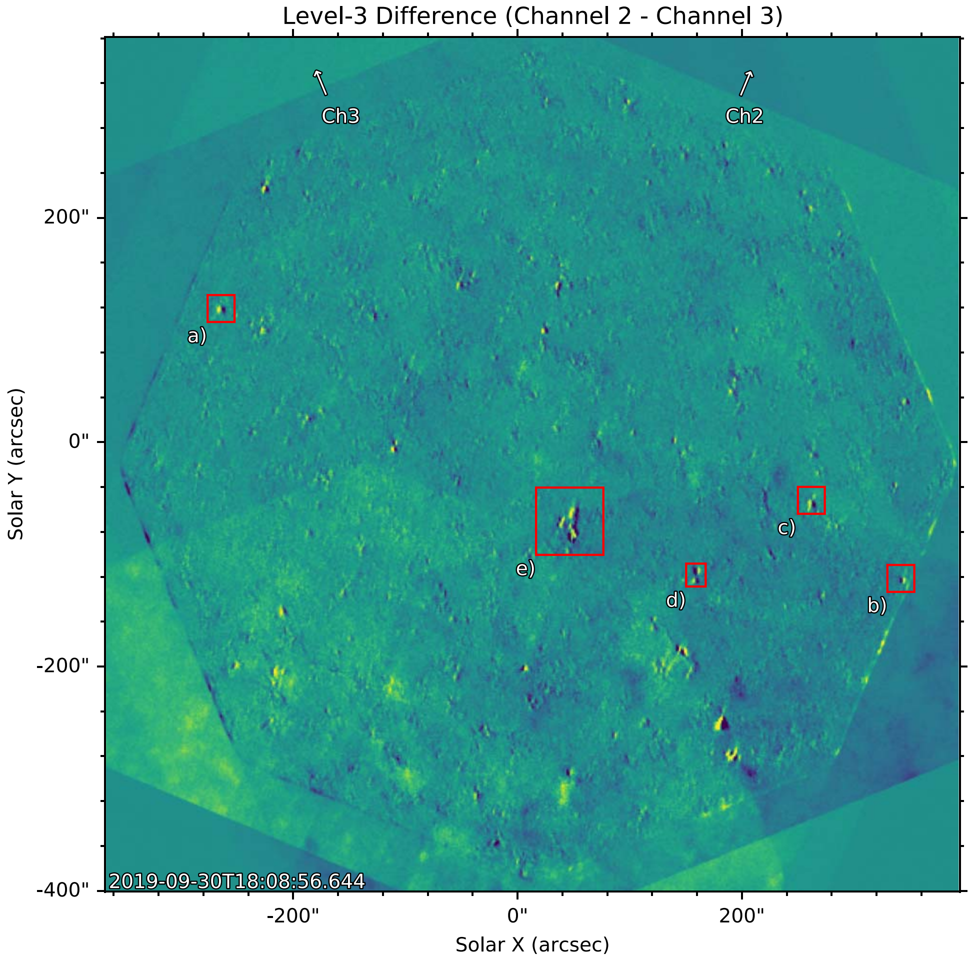

Figure 9. Full field-of-view difference between channel 2 and channel 3 level 3 images. Arrows denote the positive dispersion direction in channels 2 and 3. Events a–c are highlighted in Figure 10. Inverted results for events c and d are shown in Section 4.2. A time series of event e is shown in Figure 11. The associated animation shows these difference images throughout the ESIS observation. The animation begins on 2019 September 30 at 18:06:16.644 and ends the same day at 18:10:46.644. The real-time duration of the animation is 6 s.

(An animation of this figure is available.)

image, to account for the change in dispersion direction. ESIS level 3 images have a fixed solar coordinate; therefore, the field of view defined by the octagon drifts as a function of time index, s, due to a slight pointing drift during the flight. The empirical drifts are $[x_{\rm drift}, \ y_{\rm drift}] = [8, \ -4]$ pixels. The total number of level 3 exposures is $s_t = 29$.

In the above relations, we have just four free parameters, the slopes m_i. The four channels of ESIS give six possible difference images for fitting the vignetting function for each image sequence s. When the average slope of all 174 combinations (six difference images per each of the 29 exposures) is minimized, we consider the vignetting corrected.

Measuring the trend from the data is additionally complicated by the overlap of the bright Mg X 609.79 Å line. This line overlaps different regions of the field of view in each channel; see Figure 8. Therefore, when fitting the background, we restrict ourselves to the portion of the field of view without the Mg X 609.79 Å overlap in any channel. We only use column means between the red bars in Figure 7 to ensure sufficient pixel numbers in each column.

The resulting final fit, $m_i = [0.35, \ 0.28, \ 0.34, \ 0.6]$, differs from the field predicted using ray tracing and geometric optical models of the ideal instrument (Smart et al. 2022). Our fit required independent slopes for each channel, which are likely due to the imperfect placement of optical elements in the instrument. We also find a smaller slope (less vignetting) across the field of view. It is possible that this is due to our inability to completely remove extra intensity from overlapping spectral lines, something we will only be able to do properly when inverting the full ESIS passband. Despite these issues, our correction to the vignetting in level 3 images makes their differences much flatter in intensity postcorrection, as is seen in Figure 7(c), and will therefore lead to a higher-fidelity intensity recovery when inverting level 3 data.

3.3.4. Relative Radiometric Correction

Each channel is normalized by equalizing the image mean over the least contaminated shared piece of Sun and is therefore performed after interchannel coalignment and the vignetting correction. We divide each image by its mean in the region of the field of view uncontaminated by Mg X 609.79 Å in every channel (shape shown in Figures 7(a) and (c)) and multiplying it by the mean in that same region from the brightest image in the brightest channel (channel 2 at apogee). This normalizes the signal between each channel at every exposure and corrects for

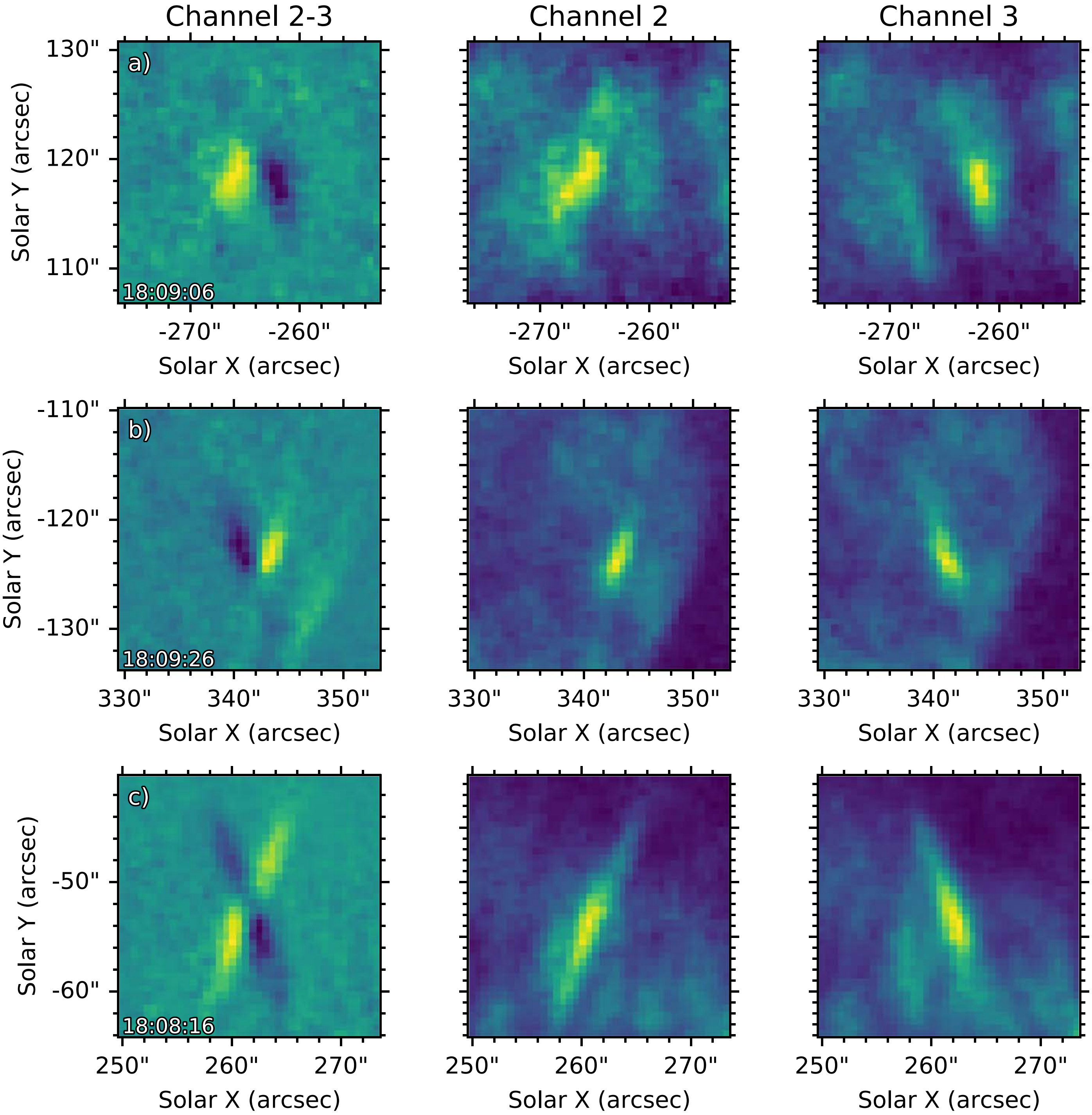

Figure 10. Events a, b and c identified in Figure 9 are examples of a mostly blue, red, and broadened event, respectively. The difference between channels 2 and 3 is shown in the left column, while the channel 2 and 3 intensities are shown in the middle and right columns. The velocity signature is most easily seen in the difference image, while the straight intensities provide information on the line core intensities.

the time-varying atmospheric absorption mentioned in earlier sections.

4. Preliminary Results

In this section, we provide a preliminary analysis of the ESIS level 3 data. Our aims are to assess the ability of the ESIS data to (1) provide velocity signatures of dynamic events and (2) aid in developing a useful qualitative and quantitative understanding of the events. Despite the lack of solar activity, ESIS managed to capture tens of small, transient events and one larger event during the ~5 minutes of observation in the O V 629.7 Å spectral line. We analyze five example events in this section.

4.1. Level 3 Difference Images

Early work with MOSES images demonstrated the utility of examining differences between different projections of the spatial–spectral cube (channels) to identify solar features with a

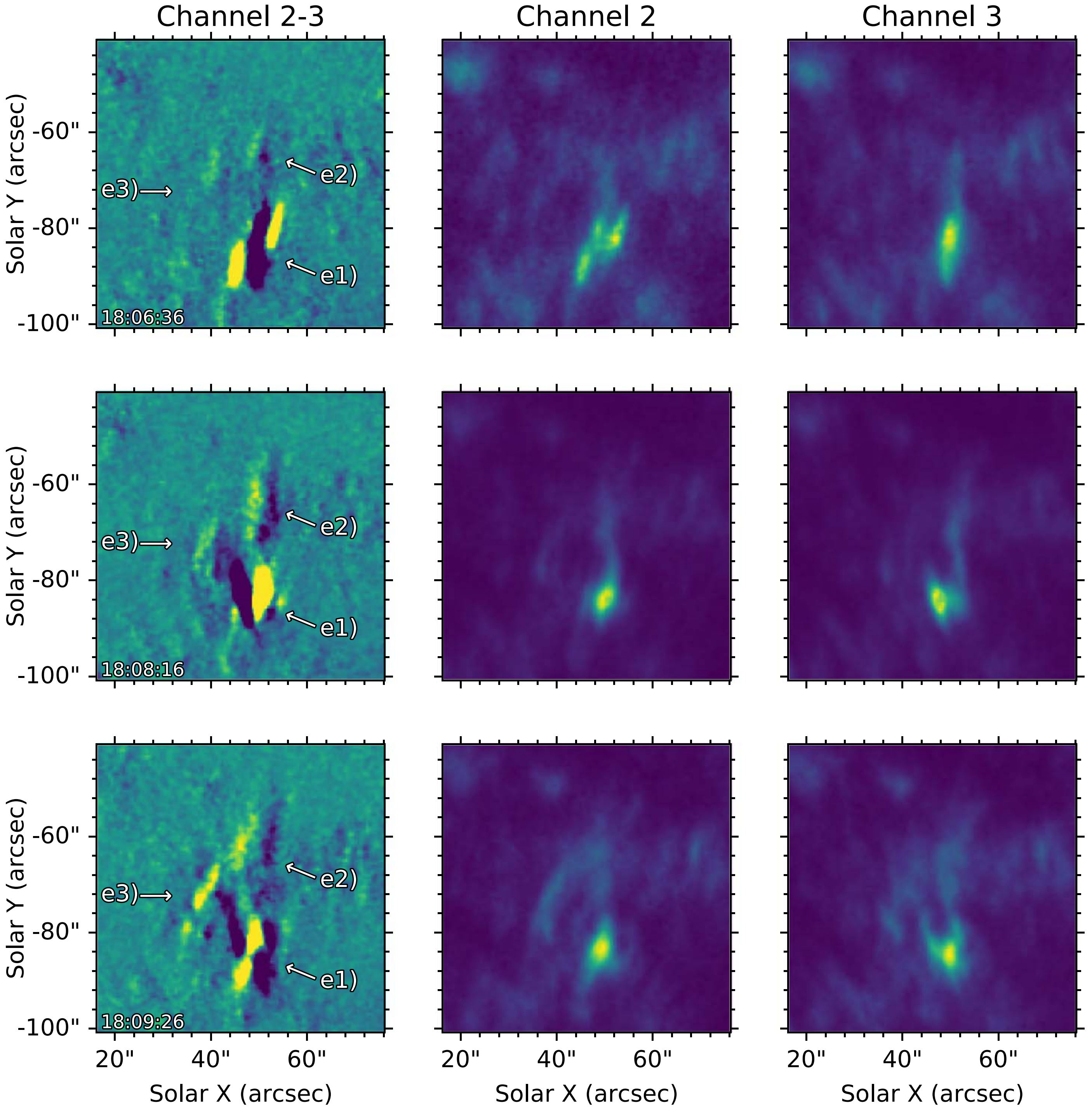

Figure 11. Largest and most complex velocity event (e) captured by ESIS shown at three different times. The event starts as two jets (one red and one blue) with slight spatial separation at location e1; evolves into a strong redshift, where the event begins paired with faint blueshifted material above (e2); and ends in a complicated combination of velocity not easily interpreted from difference images. The animation of this figure shows the complete evolution of the event with cotemporal images from AIA 304, 171, and 193 Å for additional context. The animation begins on 2019 September 30 at 18:06:16 and ends the same day at 18:10:56. The real-time duration of the animation is 6 s. Snapshots of the AIA images are also included in Figure 12.

(An animation of this figure is available.)

significant line-of-sight velocity (Fox et al. 2010; Fox 2011; Rust 2017; Rust & Kankelborg 2019) and diagnose spectral contamination (Rust 2017; Rust & Kankelborg 2019). It is for this reason that we developed a level 3 data product, spatially coaligned in O V, that would allow us to take differences between ESIS channels. Each ESIS channel disperses solar features in a different direction relative to solar north, determined by the orientation of each grating. The positive dispersion direction in each level 3 image is indicated by the arrows in Figure 8.

Figure 9 (and the associated animation) shows the difference between channels 2 and 3 for the full ESIS field of view. Since wavelength is dispersed in a different direction in each channel, taking the difference between two simultaneous, spatially

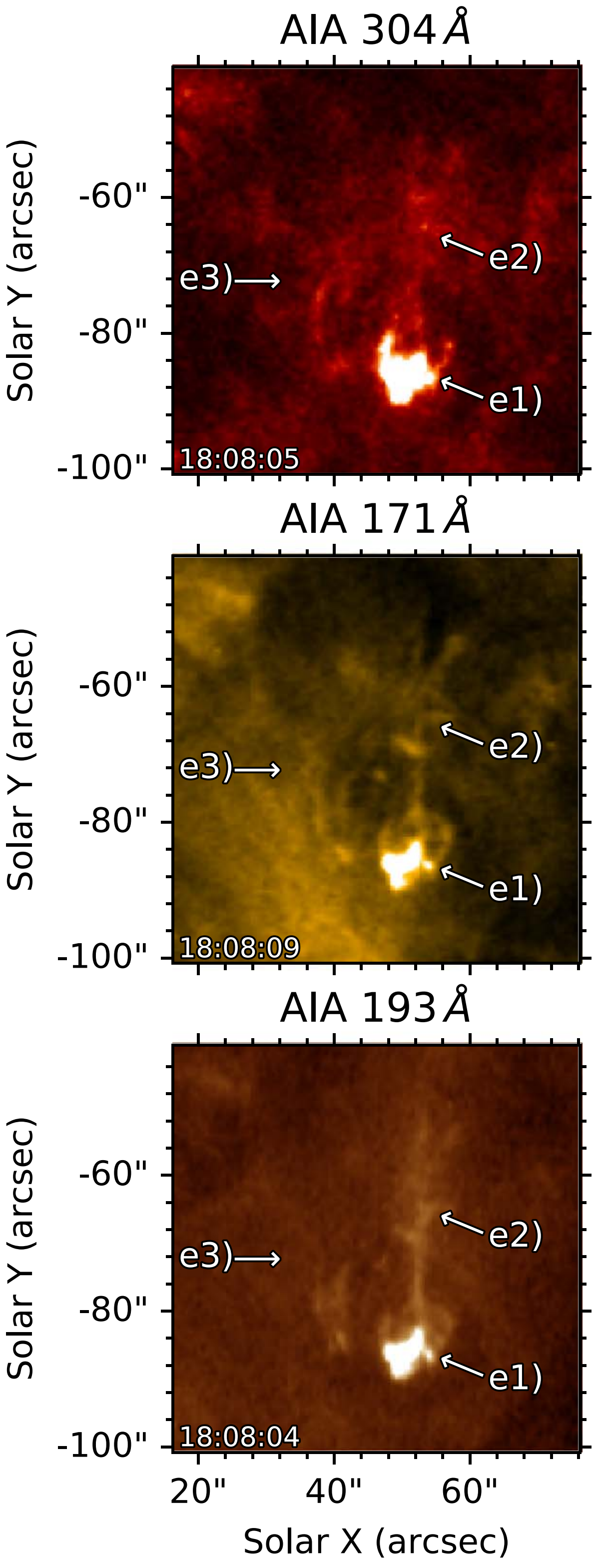

Figure 12. Coaligned AIA 304, 171, and 193 Å images of event e (highlighted in Figure 11) are shown with identical locations labeled. The location of peak intensity (e1) in the ESIS level 3 data coincides with the brightest intensity in these EUV channels. We also note a jetlike structure, which is very diffuse in the cooler 304 Å images and visible as a thin line of intensity in 171 and 193 Å between the e1 and e2 labels, that matches the location of the faint blueshifted structure visible in level 3 difference images. Animations of these AIA channels, included with Figure 11, show material traveling along this line and being ejected away from location e1.

aligned channels cancels the intensity in the O V spectral line core. What remains are signatures of Doppler shifts, line broadenings, and other spectral lines. Before we describe the signatures of Doppler shift, it may be helpful to point out certain large-scale features that arise from spectral contamination. The yellow octagon overlaid in the lower left quadrant of the image is the Mg X 609.79 Å line that overlaps the O V 629.7 Å line in channel 2. Similarly, a dark octagon in the lower right quadrant is the portion of the Mg X 609.79 Å line that overlaps the O V 629.7 Å line in channel 3.

In the difference image, small-scale black and white lobes frequently appear near the locations of bright features on the Sun. A few such features are marked with red boxes and will be discussed in detail below. The small black lobes tend to lie at an angle of −22°.5 with respect to solar north, which is the direction of dispersion of channel 3, while the white lobes tend to lie at an angle of +22°.5 with solar north, which is the direction of dispersion of channel 2. A sufficiently compact and well-isolated brightening functions as its own spectrograph slit. The lobes then form V-, Λ-, or X-shaped features. Furthermore, intersection of the lobes occurs at the line center. Lobes above that intersection (i.e., along the dispersion direction in both channels) indicate a redshift (V). Lobes below line center similarly indicate a blueshift (Λ). The complete X shape indicates a line broadening in which both red- and blueshifts are present.

Although the ESIS geometry differs significantly from MOSES, which had three images taken at spectral orders $m = -1, 0, 1$ of a single grating, analogous Doppler signatures appeared in MOSES data. These Doppler signatures were analyzed in great detail by Rust & Kankelborg (2019), who sliced through small events along the dispersion direction to measure He II 304 Å line profiles from MOSES data.

Three features, labeled a, b, and c in Figure 9, serve to illustrate the Λ, V, and X morphologies described above. Figure 10 shows the difference image in the first column for all three events, then the channels 2 and 3 data in the subsequent columns. Figure 10(a) shows a Λ-shaped event. By the reasoning given above, we immediately know that this event is predominantly blueshifted. Similarly, an upward-facing V-shaped event, like the one shown in Figure 10(b), is predominantly redshifted. The X-shaped events, shown in Figure 10(c), suggest enhanced emission in both the red and blue wing of the line profile. Difference images can provide immediate qualitative understanding of these simple, pointlike events. During the 5 minute rocket flight, tens of similar events were detected in the ESIS field of view. We observe that the X-shaped events are especially common in this data set, though multiple examples of each type are apparent.

During the ESIS flight, we also captured a handful of spatially extended Doppler signatures that are more difficult to interpret. The most obvious of these is an eruption near disk center, event e in Figure 9. This large event is shown three times in Figure 11. The entanglement of spatial and spectral information in this relatively complex event makes it difficult to derive a qualitative interpretation from the difference images (left column of the figure). A cluster of overlapping positive and negative lobes in the brightest portion of the event (location e1) sometimes presents as a Λ, V, or X shape, but not always, and evolves significantly in time. The top row shows this event early in its evolution. Intensity is concentrated in a

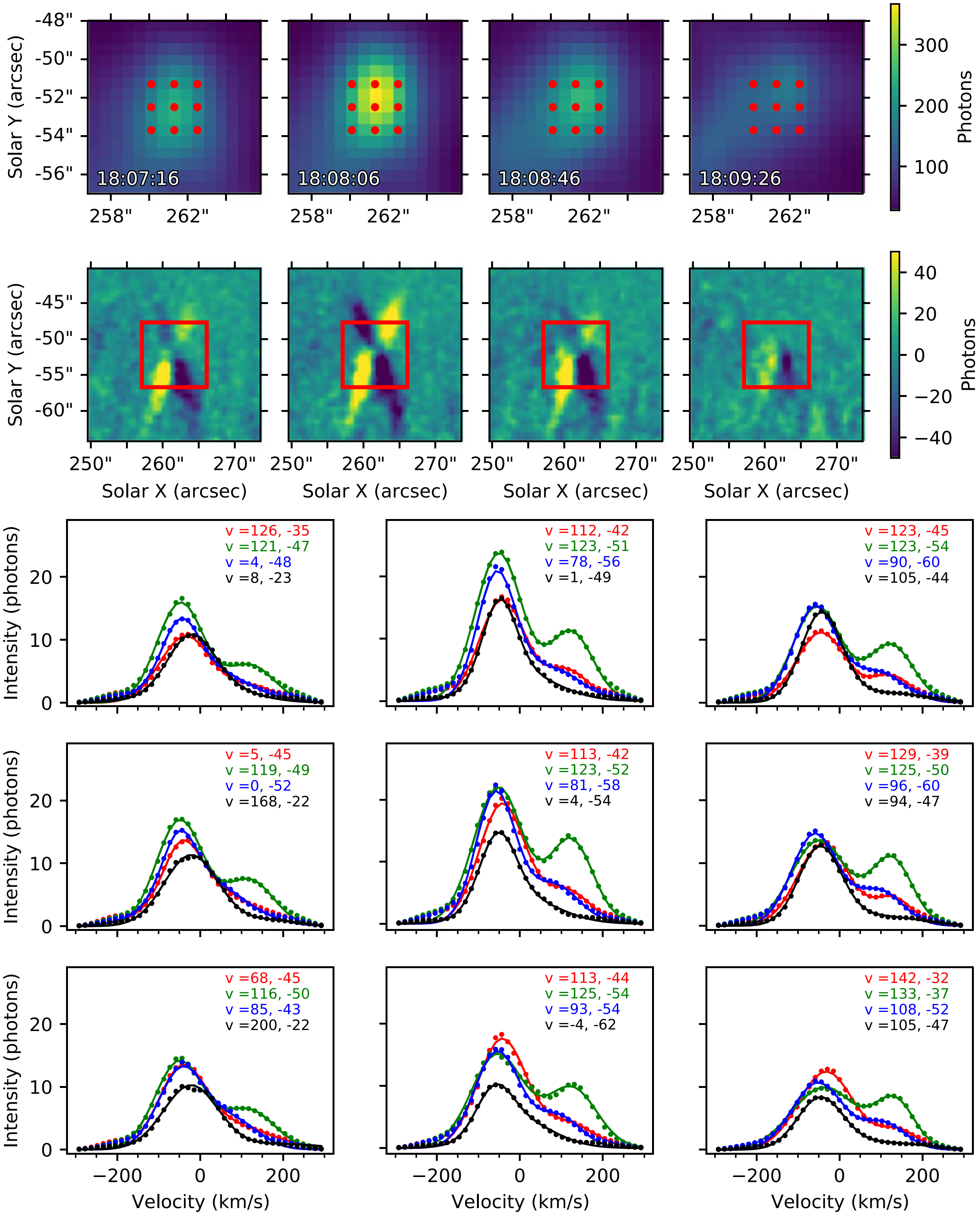

Figure 13. MART inverted results for event c in Figure 9 at four different times. The integrated intensity (top row) and corresponding level 3 difference image (second row) are shown at four different times. The red box marks the field of view used in the top row. The O V 629.7 Å line profile at each position marked with a red dot is plotted in the matching 3 × 3 grid in a different color for each time (in order: red, green, blue, and black). Each MART line profile (dots) is overplotted with a double Gaussian fit (solid lines). Bulk shifts in kilometers per second for each component of the fit are provided in the legend for each time in their respective color. The animation of this figure shows the full temporal evolution of these line profiles measured by ESIS. The animation begins on 2019 September 30 at 18:06:16 and ends the same day at 18:10:16. The real-time duration of the animation is 5 s.

(An animation of this figure is available.)

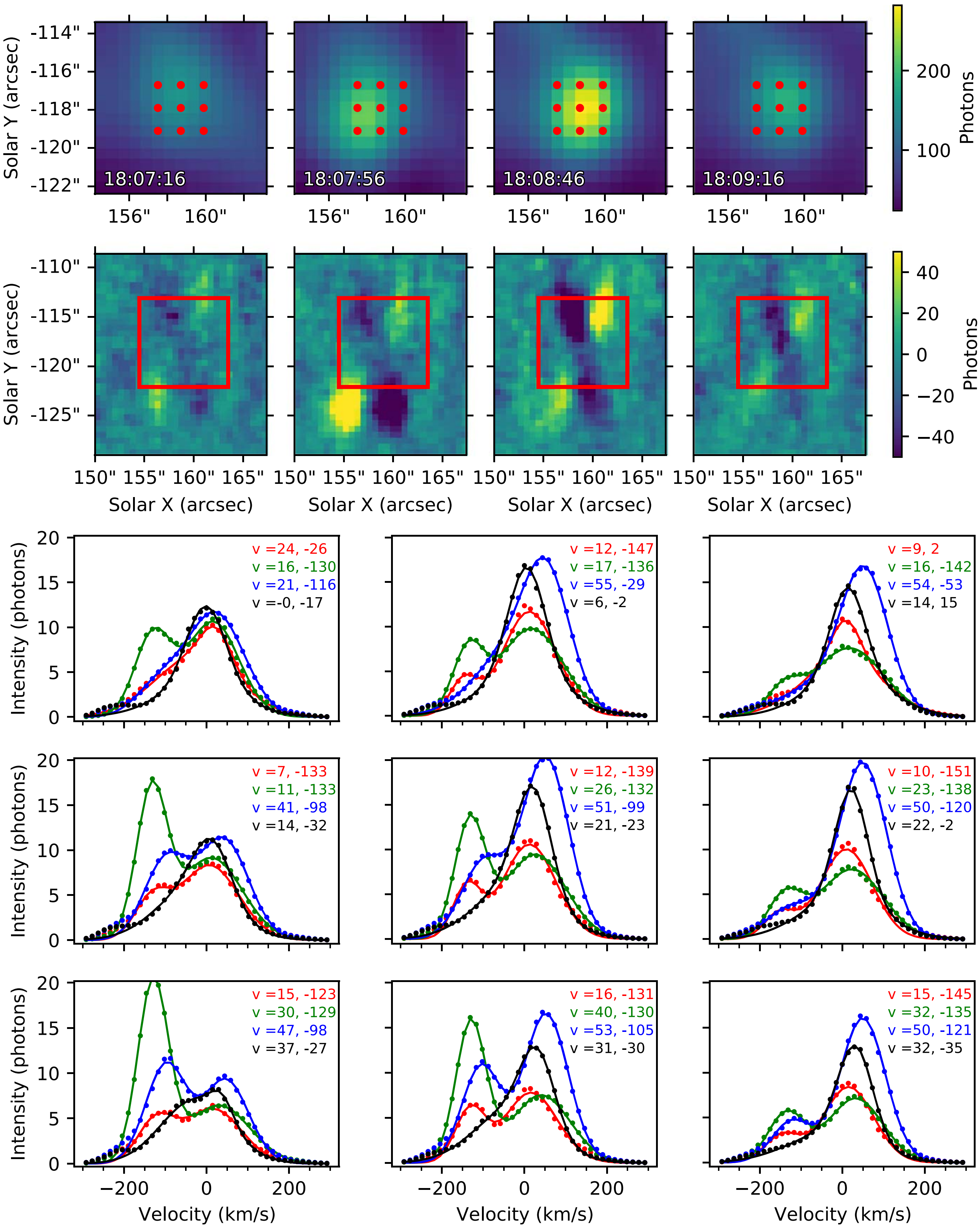

Figure 14. MART inverted results for event d in Figure 9, at four select times, presented in the same fashion as in Figure 13. The animation of this figure shows the full temporal evolution of these line profiles measured by ESIS. The animation begins on 2019 September 30 at 18:06:16 and ends the same day at 18:10:56. The real-time duration of the animation is 6 s.

(An animation of this figure is available.)

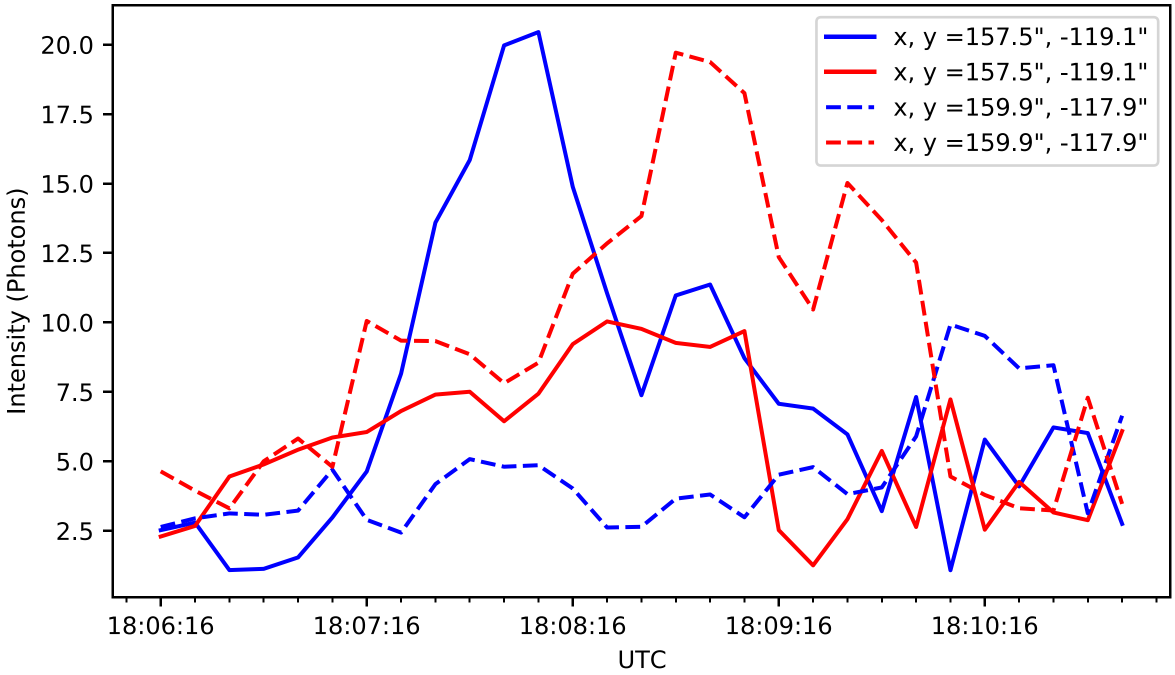

Figure 15. The peak intensities of the blue and red components of the Gaussian fit performed on the inversion of event d are shown at two different spatial locations. The peak intensities from the lower left corner dot in Figure 14, at x, $y = 157\overset{''}{.}5, -119\overset{''}{.}1$, are shown as solid lines. Those from the middle dot of the right column, x, $y = 159\overset{''}{.}9, 117\overset{''}{.}9$, are shown here as dashed lines. The time series of these peak intensities clearly shows the separation in time of each jet. It also shows the spatial separation of the red and blue jets, particularly at the position of the dashed line, where intensity from the blue portion of the event is almost completely absent.

small region and presents as two jets, one red and one blue, with the redshifted source slightly to the right of the blueshifted source. The event is dominated by a significant redshift (upward-facing V) at the location of initial brightening 100 s later (middle row). There is an imprint of fainter differences above the brightest knot of intensity (location e2) showing motion along a spatially extended structure. The difference lobes in this faint structure are opposite in polarity to the intensity below and therefore appear to represent blueshifted material ejected from the site of initial brightening. This is supported by the appearance of a thin string of ejected material at the same location in AIA 304, 171, and 193 Å (Figure 12 and the animation associated with Figure 11). By the end of the event (another 70 s later; bottom row), the dominant redshift subsides, leaving a complicated spectral signature at the brightest portion of the event and in the adjacent region up and to the left (location e3).

So far, we have been exploiting two of the four ESIS channels with our difference image. This approach is qualitative, and its limitations become apparent with complex and spatially extended dynamics, as we saw in event e. An understanding of ESIS difference images provides a starting point and offers a sanity check when interpreting numerical inversions that take advantage of all four projections. In the following section, we will focus on inverting two smaller events (c and d), and we will save a more in-depth analysis of event e for a future publication.

4.2. Early Inversions

In order to better disentangle the spectral and spatial information captured by ESIS and provide quantitative velocity information, all four channels must be combined and "inverted" to return a single spatial–spectral cube, $I(x, y, \lambda)$, at every exposure. For our preliminary inversions of the O V 629.7 Å ESIS level 3 data, we used a multiplicative algebraic reconstruction technique (MART). MART is attractive for our first inversions because it is fast, requires no training or explicit assumptions about the data, and automatically enforces image positivity. We describe our MART implementation in Appendix B.

When constructing the ESIS level 3 data, each channel is coaligned to a reference channel (Section 3.3). By doing this, we are assuming that the mean velocity in O V 629.7 Å is zero prior to inverting. Work by Peter & Judge (1999) suggests that the transition from a mean redshift to a mean blueshift at disk center occurs around 0.5 MK. Therefore, since O V 629.7 Å is a relatively hot transition region line and is formed near 0.22 MK, we expect a systematic error in our inverted velocities of less than 10 km s^{-1} as a result of this assumption.

In Figures 13 and 14 and their associated animations, we present the MART inversion for two different compact transient events, labeled c and d in Figure 9. Both events have an X-shaped presentation, begin and end within the ESIS observing time, and show noticeable temporal evolution in velocity. Each figure shows the total O V 629.7 Å integrated intensity, obtained by summing the MART inversion along the wavelength dimension, in the top row at four different times. The second row shows uninverted channel 2 and 3 level 3 difference images at those same times for comparison. The field of view of the intensity image from the top row is shown as a red box on the difference image. Inverted O V 629.7 Å line profiles are plotted in a 3 × 3 grid, corresponding to the grid of nine positions marked in red on the intensity images. The red, green, blue, and black curves correspond to the four times indicated in the top row. We performed a double Gaussian fit for each line profile in order to more easily pick out the location of each peak in the line profile and measured the associated Doppler shift of each component. The results of the fit (solid lines) are plotted over the MART inverted data (dots). The

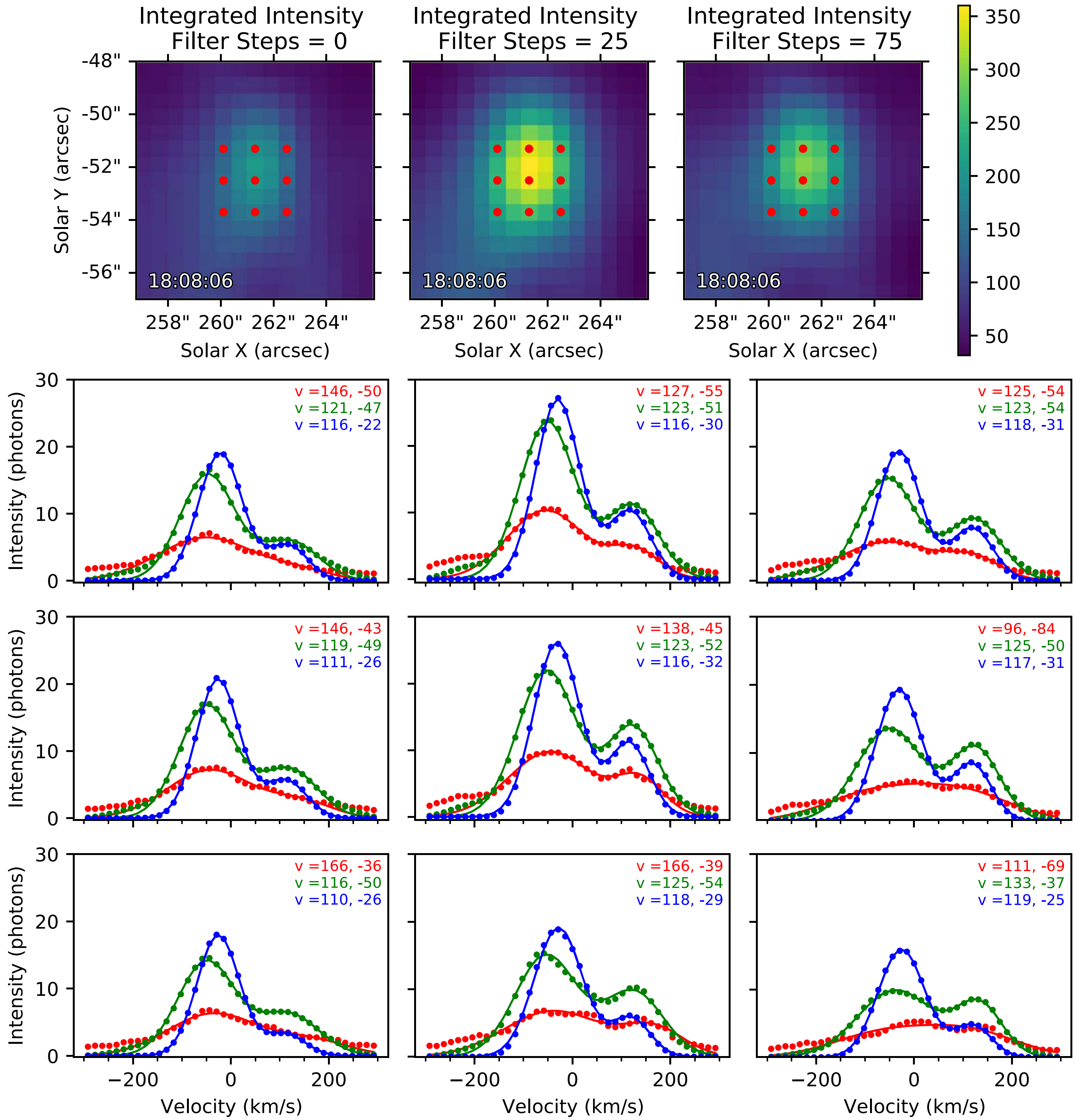

Figure 16. Comparison of MART outputs for a single time stamp in event c (Figures 9 and 13) with different amounts of filtering. The top row shows the total inverted intensity at a single time stamp each using a different number of MART filtering steps (steps 2 and 3). The lower grid shows the inverted O V spectral line at each red dot for zero, 25, and 75 filtering steps in red, green, and blue, respectively.

deviation from line center of each Gaussian is recorded in kilometers per second in the color matching the line profile. In the animation, we plot the red and blue components of each fit separately as dashed lines, their sum as a solid line in fuchsia, and the MART inverted line profile in green dots.

Event c, shown in Figure 13, lasts just over 4 minutes and shows significant temporal evolution in the line profile. Throughout the event, the blue component of the O V 629.7 Å line dominates and is centered at $\sim\!-50$ km s^{-1}. This blue component persists for the entire duration of the event with relatively gradual changes in intensity and velocity. The red component of the event is bursty in nature, with two small peaks in intensity at 18:07:36 and 18:08:16, and centered at $\sim$120 km s^{-1}. The red and blue components of the line are only occasionally well separated, but the two-Gaussian fit consistently follows the inverted line profiles with only small deviations. This explosive event is ∼3″ in diameter and shows little spatial variation in the line profile across the event.

The explosive event highlighted in Figure 14, event d, is similar to event c in that it has enhancement in both the red and blue wings of the line profile but is more complicated in its presentation. Event d begins around 18:07:16, and its intensity has almost completely died away by the last level 3 image. At the beginning of the event, a slightly redshifted component dominates the line profile. A strong blue component in the line profile centered near $-130\,\mathrm{km\,s^{-1}}$ begins to appear at 18:07:16 and peaks at 18:08:06. This blue component is brightest in the lower left portion of the event. The red component of the line profile peaks at 18:08:56 and is centered near 50 $\mathrm{km\ s^{-1}}$. Unlike event c, the blue component of the line is less persistent in time. Also, the blue and red components of the event do not occur in the same spatial location. This is visible in both the grid of line profiles and the difference images, and it is highlighted in Figure 15. Intensity in the line profiles shows the blue component peaking in the lower left, while the red component peaks in the middle to right columns. In the difference images, this corresponds to a clear vertical and horizontal separation between the blue Λ and the red V. A closer look at the inverted data shows an ∼1.″35 spatial separation between the centroids of the blue and red components.

The described MART inversions yield very smooth line profiles. This is a result of interpolation performed when coaligning the data and while rotating the spatial–spectral cube during inversions and direct smoothing applied to the cube. For this reason, our Gaussian fits match the inverted spectra exceptionally well, with very little uncertainty in the peak location of each Gaussian, and therefore measured bulk flows. Early and late in the event, where signal is insufficient, these fits break down, the Gaussians become a visibly poor fit to the inverted spectra, and the resulting measured Doppler shifts should not be trusted. This is why we focus our description only on the brightest moments in the event. For the most part, however, measurement noise is not a significant source of uncertainty in the fits. A more significant source of uncertainty in measured Doppler velocity comes from systematic effects related to adjustable parameters in the inversion. There are two free parameters in our MART algorithm, namely, the exponent used in the contrast enhancement filter and the number of times it is applied (Appendix B, steps 2 and 3). The inversions in this section were tried with a wide range of these parameters. Appendix B shows the results of tweaking these free parameters for a single time stamp of event C (Figure 16). We find that the results are robust to variation in both parameters. In particular, we consistently find line profiles consistent with a qualitative interpretation of the difference image movies and measure bulk flows (the shift in the centroid of our fitted Gaussians) within $\sim\pm15\,\mathrm{km\,s^{-1}}$ (±1 pixel) for a given exposure.

5. Discussion/Conclusions and Future Work

The ESIS sounding rocket mission, launched on 2019 September 30, was successful in capturing spatial and spectral information over its entire 11.′5 field of view in multiple wavelengths (He I 584.3, Mg X609.79, and O V 629.7 Å) at every exposure. ESIS is a unique instrument. It is a slitless imaging spectrograph, of which there only a handful of examples, and also a CTIS. To our knowledge, the ESIS and MOSES sounding rocket instruments are the only CTIS instruments ever flown in space to observe the Sun.

We have processed the ESIS data into multiple levels such that preliminary scientific work can be done, including a level 3 data product (Section 3.3) that allows for taking spatial differences between channels and early inversion. Level 3 difference images in the O V 629.7 Å wavelength (Section 4.1) reveal a host of small transient brightenings across the field of view with significant line-of-sight Doppler velocity, some in excess of $\pm100\ \mathrm{km\,s^{-1}}$. Moreover, they reveal several larger and more complex events with large velocities, most notably the eruption identified near disk center (event e in Figure 9).

We use a MART (Appendix B) to disentangle the combined spatial and spectral information in the four ESIS level 3 images to find a single spatial–spectral cube (x, y, λ), covering just the O V 629.7 Å line, for two small transient brightenings (Section 4.2). Our inversions reveal strong red and blue jets with bulk flows in excess of $100\,\mathrm{km\ s^{-1}}$ that evolve on the timescale of the ESIS cadence, 10 s. These two events are spatially compact, a few arcseconds, and have lifetimes of a few minutes. Despite their compact nature, the red and blue components measured are separate and distinct in both space and time. This is especially noticeable in event d (Figures 9 and 14), where the centroids of the blue and red jets are displaced by a little over an arcsecond.

The bimodal nature of these small brightenings is similar to observations made by Rust & Kankelborg (2019) of He II 304 Å using MOSES data, particularly in the case of event d, where the separation is visible in the level 3 data prior to inversion. This presentation is different than the typical explosive event line profiles typically observed by IRIS in Si IV 1394 Å, where small transient events often show smaller bulk flows, dominant line core emission, and nonthermal broadening (Innes et al. 2015; Chitta et al. 2017). The bimodal profile and bulk flows exceeding the sound speed ($\sim78\,\mathrm{km\,s^{-1}}$ for O V at 225,000 K) suggest magnetic reconnection occurring in a small region with little to no stationary emitting plasma, most reminiscent of a Petschek-type reconnection (Innes & Tóth 1999). Though we hypothesize that both jets originate at a single reconnection site, we admit that it is puzzling that the observed fluctuations of the red and blue jets are not temporally correlated, most notably in explosive event d (Figure 14). It is likewise puzzling that in both events c and d, there is a lack of symmetry in velocity between the red and blue jets. It may be that the reconnection in these small events is more complex than we imagine and needs to be treated in three dimensions; however, it is possible that, looking in a single spectral line, we are not seeing all of the ejected plasma. Further work with the ESIS data may help to clarify this issue. Several of these events were captured in He I 584.3, Mg X609.79, and O V 629.7 Å simultaneously, putting ESIS in a position to measure the outflows at multiple temperatures. If the event is present in hotter or cooler lines, we can see if the bimodal nature of these line profiles persists at lower and higher temperatures. Also, IRIS was running small four-step coarse rasters near disk center during the hour-long ESIS launch window. Although none of the events analyzed in this paper were captured by IRIS, a closer look at the IRIS data may reveal small explosive events suitable for direct comparison with ESIS line profiles.

The largest event captured by ESIS (Figures 11 and 12) most notably shows a strong redshift at the brightest part of the event (location e1) and a faint string of blueshifted material (location e2) rising above. The faint blueshift, combined with the appearance of rising material in the cooler AIA channels, gives the appearance of a small jet or possible mini-filament eruption. The brightest part of the event being redshifted matches the idea that “jet bright points,” a common feature of smaller jets found at the base of the erupting structure, are the result of a small postreconnection arcade (see Sterling et al. 2015, and references therein). The ability of ESIS to capture velocity information across this dynamic event at a 10 s cadence gives us a great advantage when trying to understand the underlying physics and is an exciting opportunity for future study and collaboration. Future work on this event will focus on comparing multiple inversion methods and examining multiple spectral lines in the ESIS passband to ensure we have the clearest possible picture of the velocity distribution before drawing conclusions.

The next major tasks in the analysis of ESIS data will be to invert the entire spatial–spectral cube from He II 584 to O V 630 Å. A self-consistent inversion will be required to separate out the dimmer Mg X624.9 Å and perhaps even the faint O III 599.6 Å lines. This will require a careful characterization of the wavelength-dependent distortion in the images, which is currently underway. Future multiwavelength inversions of the ESIS data will allow for more accurate estimates of the frequency and distribution of explosive events across a large portion of the solar disk and at different heights in the solar atmosphere. This will allow us to track energy and material moving through multiple layers of the solar atmosphere to form a clearer picture of where and how these reconnection events unfold.

During the roughly 5 minutes of observing time, ESIS captured tens of events with supersonic velocities, evolving on 10 s timescales, over its 11.′5 field of view, a feat no other currently operating solar instrument is capable of. A closer look at the ESIS data revealed that even seemingly simple explosive events evolve fast enough in time and have significant spatial distributions of intensity and velocity such that rastering a traditional slit spectrograph would fail to capture the event completely, possibly skewing the interpretation of the data. This, combined with the fact that ESIS can and did measure many events like this simultaneously, makes it a powerful tool for capturing and diagnosing dynamic events in the solar atmosphere. We believe this first flight of ESIS successfully demonstrated the viability of CTIS style instruments for studying solar transients and that the solar physics community should continue to pursue the technology and implement it in future missions.

This work was supported primarily by NASA grant NNX14AK71G. R.T.S. acknowledges NASA NESSF program grant 80NSSC17K0524. The success of ESIS owes much to the technical skill of personnel at NASA Marshall Space Flight Center, particularly Ken Kobayashi, Brent and Dyana Beabout, Harlan Haight, and James Duffy. We would also like to acknowledge the NASA SRPO and NSROC employees involved, all of whom went above and beyond to support ESIS from start to finish; we could not have done it without you. CHIANTI is a collaborative project involving George Mason University, the University of Michigan (USA), the University of Cambridge (UK), and NASA Goddard Space Flight Center (USA). This research used version 0.5.0 (doi:10.5281/zenodo.4676478) of the aiapy open-source software package (Barnes et al. 2020).

Appendix A
Despiking

We developed a new image despiking algorithm with a spike intensity threshold that varies according to the local median intensity. The key to our strategy is to establish a finite number of bins for the local median intensity and then examine the statistics of all of the pixels falling into each bin. Our despiking routine is implemented in the following steps.

1. For each data dimension (image row, image column, and time), calculate a local median intensity image by averaging the nearest 11 pixels along the given axis. Divide the range of median image values into 128 bins.
2. For each local median bin, form a cumulative distribution of intensities. Identify the intensity value corresponding the 99.9th percentile. The result is three curves (one for each data dimension) of 128 points each.
3. For each data dimension, fit a line to the threshold curve. The line identifies the relationship between median intensity and spike threshold for that dimension.
4. Create three masks, which are Boolean-valued images identifying pixel values that exceed the thresholds, one image per data dimension.
5. Combine the three masks with logical AND to produce the final map of bad pixels (spikes).
6. Replace each bad pixel with a local mean of good (i.e., not bad) pixels only, weighted by kernel k (Equation (A1)).

The kernel used to determine the replacement value for bad pixels is

$$k(x, y, t) = e^{-\{|x|+|y|+|t|\}/a}. \tag{A1}$$

For our implementation, $a = 0.5$ pixels, and $x, y, t = -2, -1, 0, 1, 2$. The kernel is normalized prior to application by it is total, ignoring any other bad pixels that may fall within the kernel.

The algorithm described above has a number of advantages compared to those available in standard data prep routines for solar physics missions. We are aware of only one published example of a despiker that uses the time axis for spike identification, used by Aschwanden et al. (2000) on data from the Transition Region and Coronal Explorer (Handy et al. 1999), though other sophisticated despikers have been used in processing data from SECHI/STEREO (Howard et al. 2008) and MDI (DeForest et al. 2007).

In our algorithm, a pixel must stand out from its neighbors in all three dimensions to be identified as a spike. This criterion reduces false positives; yet because of this approach, we can choose a relatively sensitive percentile threshold based on image statistics to reduce false negatives. Usually, a percentile-based threshold would result in identifying a fixed number of bad pixels, but since the logical AND is nonlinear with respect to the three binary masks, it is possible to identify a small or large number of spikes in a given image. For example, with our 99.9th percentile threshold, the algorithm can find as few as zero or as many as 2129 bad pixels in a 2048 × 1040 level 1 image.

Appendix B
Multiplicative Algebraic Reconstruction Technique

The MART was developed for limited-angle tomography problems, in which a small number of projections are used to reconstruct a volume (Okamoto & Yamaguchi 1991; Verhoeven 1993). As ESIS has only four projections through the (x, y, λ) volume, it is a good candidate for this approach. When testing a variety of inversion methods on MOSES data, Fox (2011) identified MART as the most promising of several methods in terms of speed and fidelity. Rust (2017) applied a slightly different version of MART to the MOSES data paired with a wavelet-based partial reconstruction technique for better background subtraction and event isolation. Due to its speed, simplicity, and automatic enforcement of image positivity, we have chosen MART for our first inversion of level 3 ESIS data.

With MART, we seek to reconstruct the true spatial–spectral cube, $I_{xy\lambda}$, using all four ESIS images from a single exposure. Each ESIS image, $i_{\theta x'y'}$, can be expressed as an angled projection through $I_{xy\lambda}$ onto a two-dimensional detector, or

$$i_{\theta x'y'} = \sum_{\lambda} I_{\theta x'(y'-\delta\lambda)\lambda}, \qquad \text{(B1)}$$

where

$$I_{\theta x'y'\lambda} = \mathcal{R}_{\lambda}(\theta) I_{xy\lambda}, \qquad \text{(B2)}$$

and $\mathcal{R}_{\lambda}(\theta)$ is a rotation about the λ-axis into the primed detector coordinates $[x', y']$. In this rotated system, y' is the dispersion direction. There is one ESIS image for each $\theta \in \{-67\overset{\circ}{.}5, -22\overset{\circ}{.}5, 22\overset{\circ}{.}5, 67\overset{\circ}{.}5\}$, representing the orientations of each ESIS channel. Projections through I are done along lines of constant $y' - \delta\lambda$. For our specific implementation, the resolution of $I_{xy\lambda}$ in λ is chosen to be $28\,\text{mÅ pixel}^{-1}$, the spectral dispersion of an ESIS grating, such that $\delta = 1$.

MART attempts to find the true spatial–spectral cube $I_{xy\lambda}$ by iteratively correcting a guess cube, $G_{xy\lambda}$, until its projected images, $g_{\theta x'y'}$, match each ESIS image, $i_{\theta x'y'}$, with a reduced χ^2, $\chi^2_{R,\theta}$, less than 1. Our procedure is as follows.

1. Create a guess cube, initialized as $G_{xy\lambda} = 1$, on the same domain as I.
2. Enhance the contrast of G and normalize:

   $$G \leftarrow \frac{G + G^{(1+\Psi)}}{\sum_{xy\lambda} G + G^{(1+\Psi)}} \sum_{xy\lambda} G. \qquad \text{(B3)}$$

3. Convolve G with a smoothing kernel K, $G \leftarrow G^{*}K$, in our case,

   $$K_{ijk} = \frac{2^{3-|i|-|j|-|k|}}{64} \quad \text{for} \quad i, j, k = -1, 0, 1. \qquad \text{(B4)}$$

4. Assuming $\delta = 1$, sum $G_{\theta x'y'\lambda}$ along lines of constant $y' - \lambda$ to calculate a projection for each angle θ,

   $$g_{\theta x'y'} = \sum_{\lambda} G_{\theta x'(y'-\lambda)\lambda}, \qquad \text{(B5)}$$

   where

   $$G_{\theta x'y'\lambda} = \mathcal{R}_{\lambda}(\theta) G_{xy\lambda}, \qquad \text{(B6)}$$

   and $\mathcal{R}_{\lambda}(\theta)$ is a rotation about the λ-axis.
5. Calculate reduced chi-squared and check for each channel for convergence, in this case that $\chi^2_{R,\theta} < 1$,

   $$\chi^2_{R,\theta} = \frac{1}{N_{x'}N_{y'}} \sum_{x'y'} \frac{(i_{\theta x'y'} - g_{\theta x'y'})^2}{g_{\theta x'y'} + \sigma^2_{\mathrm{RN}}}, \qquad \text{(B7)}$$

   where σ_{RN} is the read noise in photons, and $N_{x'}$ is the total number of elements along x'.
6. Calculate correction factors for each unconverged channel, θ_{uc}, weighted by γ,

   $$c_{\theta x'y'} = \left[\frac{g_{\theta x'y'}}{i_{\theta x'y'}}\right]^{\gamma}, \qquad \text{(B8)}$$

   where $\gamma = 2/n$ with n equal to the total number of channels.
7. Assign correction factors to lines of constant $y' - \lambda$ in the volume (x', y', λ),

   $$C_{\theta x'(y'-\lambda)\lambda} = c_{\theta x'y'} \qquad \text{(B9)}$$

8. Apply a weighted product of each derotated correction to G,

   $$G \leftarrow G\{\prod_{\theta \in \Theta_{\mathrm{uc}}} \mathcal{R}_{\lambda}(-\theta) C_{\theta x'y'\lambda}\}^{1/m_{\mathrm{uc}}}, \qquad \text{(B10)}$$

   where m_{uc} is the total number of unconverged channels, and Θ_{uc} denotes the set of unconverged channels.
9. Repeat steps 4–8 until every channel has converged at step 5. Once converged, proceed to next step.
10. Return to step 2 if additional filtering is desired.

The above algorithm begins with an arbitrary, flat guess (step 1). The guess is rapidly modified to fit the data projections $i_{\theta x'y'}$ by steps 4–8, which project through the guess, compare the results to the data, and calculate and apply intrinsically positive correction factors. When applied to ESIS level 3 data, the total number of channels is $n = 4$. The rotations $\mathcal{R}_{\lambda}(\pm\theta)$ cause ringing due to the Gibbs phenomenon associated with resampling and interpolation. All negative values resulting from this ringing are set to zero. In our case, the ringing occurs mostly at the sharp discontinuity at the edge of the field stop octagon.

The inversion is ill posed, in the sense that multiple different $G_{xy\lambda}$ cubes can satisfy $\chi^2_{R,\theta} < 1$. In particular, tomographic inversion algorithms such as MART tend to smear intensity along the projection directions (Kak & Slaney 2001). This tendency is especially strong when there are only a few projections. This smearing results in rapid convergence to an intensity distribution in the volume that matches the projection data but results in artificial streaks that intersect and produce anomalous bright sources. Since the resulting artifact forms a grid-like pattern of enhancements, we use the nickname "plaid" to describe it. In the reconstructed ESIS data cube, the plaid artificially enhances the wings of the spectral line wherever projections through unrelated intense sources happen to meet. To suppress the plaid, we implement an outer filtering loop that enhances the contrast of $G_{xy\lambda}$ and applies smoothing prior to the MART corrections to further constrain our inversions. The contrast enhancement (step 2) works to suppress the intensity of the artifacts and redistribute their intensity into the brightest features. We aim thereby to arrive at a solution with the fewest sources that are consistent with the appearance of the data. By itself, the contrast enhancement can tend to develop excess power at the Nyquist frequency and (sometimes) numerical instability. These undesired effects of contrast enhancement are suppressed by a smoothing filter (step 3).

As a result of the plaid suppression technique described above, our implementation of MART has two free parameters, namely, the contrast enhancement exponent Ψ and the number of times the filtering step (steps 2 and 3) is applied. In order to better understand the impact of these two parameters on our inversions, we inverted a single exposure of event c (Figures 9 and 13) using several different values of each free parameter. During this exercise, we found that lowering Ψ resulted in faster MART convergence but required more applications of the filtering step to minimize the plaid. Increasing Ψ lowered the number of required filtering loops but increased the convergence time of each MART iteration and quickly led to overfiltered and artificial-looking results. For smaller values of Ψ, less than approximately 0.4, we find Ψ to be nearly degenerate with the number of filtering steps; i.e., inversions found using a lower Ψ and more filtering steps are similar to those found using a higher Ψ and less filtering steps. In the end, we chose to use $\Psi = 0.2$ in an effort to not overfilter our inversions and maintain a reasonable total algorithm convergence time.

Figure 16 shows the results of changing the total number of filtering steps with $\Psi = 0.2$. While other numbers of filtering steps were tried, the inverted results after zero, 25, and 75 steps sufficiently illustrate the effect of varying this parameter. The impact of plaid is most evident in the red spectral lines in Figure 16, where the contrast enhancement filter was not used at all. Despite excess intensity in the wings of the lines from excessive plaid, the brightest pixels are still double peaked in nature, and the two Gaussian fits reasonably approximate the inverted line profiles. The blue spectral lines in Figure 16 correspond to 75 filtering steps, after which point the filtering has converged, in the sense that further filtering iterations have no effect. Since the contrast enhancement filter is designed to pull intensity from the background and into regions of stronger signal, it has the effect of clumping the intensity into a smaller area. This causes much less intensity in the far wings of the line profile and narrower peaks overall. Unfortunately, this also has the ill effect of clumping background intensity where there is very little signal. In low-signal regions, where we would expect a relatively flat, low-intensity, and noisy line profile, overfiltering can cause what little intensity is there to clump together artificially far out in the wings of the line. Therefore, we choose to compromise and run the filtering step enough times, in our case 25, such that the majority of the artificial intensity in the wings has been beaten down, but not so much that we artificially remove a flat noisy line profile in low-signal regions.

Regardless of the parameters chosen, we find that our inverted results match qualitative interpretations of the ESIS difference images. The degree of filtering affects the breadth of the individual Gaussian components, so that they are more or less resolved. Their velocities and relative intensities also vary but are less affected. An extreme parameter range was explored, from no filtering to maximal (fully converged) filtering. We have argued that both extremes represent implausible solutions on physical grounds. Consequently, we conclude that the relative velocities and intensities of the double Gaussian fits are robust, while their widths are uncertain.

The final configuration we used when inverting all level 3 data used 25 filtering steps and a contrast enhancement exponent of $\Psi = 0.2$. In this configuration, a single exposure of a small region like event c (with final inverted dimensions of $[x, y, \lambda] = [140, 140, 41]$ pixels) can be inverted in ∼75 s on a single thread of a four-core 2.8 GHz processor. Since the inversion of each ESIS exposure is independent, inversions can be done on multiple threads to increase efficiency when inverting additional exposures.

ORCID iDs

Jacob D. Parker https://orcid.org/0000-0001-8732-8284
Roy T. Smart https://orcid.org/0000-0002-9997-5515
Charles Kankelborg https://orcid.org/0000-0002-1992-7469
Amy Winebarger https://orcid.org/0000-0002-5608-531X
Nelson Goldsworth https://orcid.org/0000-0002-6787-0380

References

Aschwanden, M. J., Nightingale, R. W., Tarbell, T. D., & Wolfson, C. J. 2000, ApJ, 535, 1027
Barnes, W. T., Cheung, M. C. M., Bobra, M. G., et al. 2020, JOSS, 5, 2801
Calabretta, M. R., & Greisen, E. W. 2002, A&A, 395, 1077
Chamberlin, P. C., Woods, T. N., Eparvier, F. G., & Jones, A. R. 2009, Proc. SPIE, 7438, 743802
Chitta, L. P., Peter, H., Young, P. R., & Huang, Y. M. 2017, A&A, 605, A49
Courrier, H. T., & Kankelborg, C. C. 2018, JATIS, 4, 018001
Culhane, J. L., Harra, L. K., James, A. M., et al. 2007, SoPh, 243, 19
De Pontieu, B., Title, A. M., Lemen, J. R., et al. 2014, SoPh, 289, 2733
DeForest, C., Elmore, D. F., Bradford, M. P., Elrod, J., & Gilliam, D. L. 2004, ApJ, 616, 600
DeForest, C. E., Hagenaar, H. J., Lamb, D. A., Parnell, C. E., & Welsch, B. T. 2007, ApJ, 666, 576
Del Zanna, G., & Young, P. R. 2020, Atoms, 8, 46
Dere, K. P., Bartoe, J. D. F., & Brueckner, G. E. 1989, SoPh, 123, 41
Dere, K. P., Bartoe, J. F., Brueckner, G. E., Ewing, J., & Lund, P. 1991, JGR, 96, 9399
Dere, K. P., Landi, E., Mason, H. E., Monsignori Fossi, B. C., & Young, P. R. 1997, A&AS, 125, 149
Descour, M., & Dereniak, E. 1995, ApOpt, 34, 4817
Fox, J. L. 2011, PhD thesis, Montana State Univ.
Fox, J. L., Kankelborg, C. C., & Thomas, R. J. 2010, ApJ, 719, 1132
Golub, L., Cheimets, P., DeLuca, E. E., et al. 2020, JSWSC, 10, 37
Gontikakis, C., & Winebarger, A. R. 2012, in 10th Hellenic Astronomical Conference, ed. I. Papadakis & A. Anastasiadis, 11
Handy, B. N., Acton, L. W., Kankelborg, C. C., et al. 1999, SoPh, 187, 229
Harra, L., Matthews, S., Long, D., et al. 2020, SoPh, 295, 34
Harra, L. K., Hara, H., Doschek, G. A., et al. 2017, ApJ, 842, 58
Howard, R. A., Moses, J. D., Vourlidas, A., et al. 2008, SSRv, 136, 67
Innes, D. E., Brekke, P., Germerott, D., & Wilhelm, K. 1997, SoPh, 175, 341
Innes, D. E., Guo, L. J., Huang, Y. M., & Bhattacharjee, A. 2015, ApJ, 813, 86
Innes, D. E., & Tóth, G. 1999, SoPh, 185, 127
Kak, A., & Slaney, M. 2001, Principles of Computerized Tomographic Imaging, Classics in Applied Mathematics (Society for Industrial and Applied Mathematics) (Piscataway, NJ: IEEE Press)
Kankelborg, C. C., & Thomas, R. J. 2001, Proc. SPIE, 4498, 16
Keenan, F. P., Aggarwal, K. M., Berrington, K. A., & Widing, K. G. 1988, ApJ, 327, 473
Keenan, F. P., Aggarwal, K. M., Bloomfield, D. S., Msezane, A. Z., & Widing, K. G. 2006, A&A, 449, 1203
Kosugi, T., Matsuzaki, K., Sakao, T., et al. 2007, SoPh, 243, 3
Lemen, J. R., Title, A. M., Akin, D. J., et al. 2012, SoPh, 275, 17
Mariska, J. T., & Dowdy, J. F. J. 1992, ApJ, 401, 754
Okamoto, T., & Yamaguchi, I. 1991, OptL, 16, 1277
Peter, H., & Judge, P. G. 1999, ApJ, 522, 1148
Rust, T., & Kankelborg, C. C. 2019, ApJ, 877, 59
Rust, T. L. 2017, PhD thesis, Montana State Univ.
Schmelz, J. T., Reames, D. V., von Steiger, R., & Basu, S. 2012, ApJ, 755, 33
Smart, R. T., Courrier, H. T., Parker, J. D., et al. 2022, ApJ, in press
Sterling, A. C., Moore, R. L., Falconer, D. A., & Adams, M. 2015, Natur, 523, 437

Tayal, S. S., Henry, R. J. W., Keenan, F. P., McCann, S. M., & Widing, K. G. 1989, ApJ, 343, 1004
Tian, H. 2017, RAA, 17, 110
Tousey, R., Bartoe, J. D. F., Bohlin, J. D., et al. 1973, SoPh, 33, 265
Verhoeven, D. 1993, ApOpt, 32, 3736
Wilhelm, K., Curdt, W., Marsch, E., et al. 1995, SoPh, 162, 189
Winebarger, A. R., Weber, M., Bethge, C., et al. 2019, ApJ, 882, 12
Zhitnik, I. A., Kuzin, S. V., Oraevskii, V. N., et al. 1998, AstL, 24, 819